2021

Calibration-free complementary relationship estimates terrestrial evapotranspiration globally

N. Ma

J. Szilagyi
University of Nebraska - Lincoln

Y. Zhang

AGU ADVANCING EARTH AND SPACE SCIENCE

Water Resources Research

RESEARCH ARTICLE
10.1029/2021WR029691

Calibration-Free Complementary Relationship Estimates Terrestrial Evapotranspiration Globally

Ning Ma[1], Jozsef Szilagyi[2,3], and Yongqiang Zhang[1]

[1]Key Laboratory of Water Cycle and Related Land Surface Processes, Institute of Geographic Sciences and Natural Resources Research, Chinese Academy of Sciences, Beijing, China, [2]Department of Hydraulic and Water Resources Engineering, Budapest University of Technology and Economics, Budapest, Hungary, [3]Conservation and Survey Division, School of Natural Resources, University of Nebraska-Lincoln, Lincoln, NE, USA

Key Points:

- A global, 30-years-plus complementary relationship evapotranspiration (ET) product is developed and validated at the plot and basin scales
- This new ET product, derived from a minimal number of inputs without vegetation or soil data, may improve upon previous global ET estimates
- Global terrestrial ET rates increased significantly during 1982–2016, particularly in the Northern Hemisphere

Supporting Information:

Supporting Information may be found in the online version of this article.

Correspondence to:

N. Ma and Y. Zhang,
ningma@igsnrr.ac.cn;
zhangyq@igsnrr.ac.cn

Citation:

Ma, N., Szilagyi, J., & Zhang, Y. (2021). Calibration-free complementary relationship estimates terrestrial evapotranspiration globally. *Water Resources Research*, *57*, e2021WR029691. https://doi.org/10.1029/2021WR029691

Received 24 JAN 2021
Accepted 27 JUL 2021
Corrected 21 MAY 2022

This article was corrected on 21 MAY 2022. See the end of the full text for details.

Abstract While large-scale terrestrial evapotranspiration (ET) information is essential for our understanding of the Earth's water and energy cycles, substantial differences exist in current global ET products due partly to uncertainties in soil- and vegetation-related parameters and/or precipitation forcing. Here a calibration-free complementary relationship (CR) model, driven purely by routine meteorological forcing (air and dew-point temperature, wind speed, and net radiation), mainly from ERA5, was employed to estimate global ET rates during 1982–2016. Modeled ET agrees favorably with (a) monthly eddy-covariance measurements of 129 global FLUXNET sites, and; (b) water-balance-derived ET of 52 basins at the multiyear mean and annual scales. Additional evaluations demonstrate that the CR is very competitive, in comparison with other 12 widely used global ET products. The 35-years mean global land ET rate from the CR is 500 ± 6 mm yr^{-1} ($72.3 \pm 0.9 \times 10^3$ km^3 yr^{-1}) with more than 70% of the land area exhibiting increasing annual ET rates over the study period. Globally, CR ET significantly increased at a rate of 0.31 mm yr^{-1} during 1982–2016, suggesting a 2.2% increase in global land ET over last 35 years. Model inter-comparisons indicate that global annual CR ET values and their trend are close to the median of not only the 12 ET products chosen but also that of 20 CMIP6 models. Since this calibration-free CR model requires no precipitation (except in sea-shore deserts for a subsequent ET correction), vegetation or soil data, it could be incorporated into complex hydrological and/or climate models, thereby facilitating large-scale hydrological and climate simulations.

1. Introduction

Unlike precipitation and runoff which are relatively easy to measure, terrestrial evapotranspiration (ET) is one of the most uncertain components in the hydrological cycle leading to great challenges in not only in-situ observations but also in modeling (Brutsaert, 2005; Chen & Liu, 2020; Fisher et al., 2017). While a great amount of community efforts by global (e.g., FLUXNET, Baldocchi et al., 2001), national (e.g., AmeriFlux, Novick et al., 2018), and regional (e.g., HiWATER, Li et al., 2013) networks have substantially improved our understanding of the ET process over multiple ecosystems via intensified eddy-covariance (EC) data sharing and collaborations, the current EC towers are unequally distributed across the world and the data coverage for most of them are limited to less than a decade (Baldocchi, 2020; Pastorello et al., 2020). As a result, modeling approaches remain essential for characterizing ET at larger spatial (e.g., global) and longer temporal (e.g., decadal) scales.

While a wide range of global ET products have been developed by a variety of models with different scopes and complexities, substantial uncertainties still exist in not only the absolute values (Miralles et al., 2016; Mueller et al., 2011; K. Zhang et al., 2019) but also in the long-term trends of ET (Kim et al., 2021; Mueller et al., 2013; Zeng, Peng, & Piao, 2018). For example, a synthesis of 41 ET products by Mueller et al. (2011) showed that the global mean ET rate over vegetated land ranges from ca. 1.2 to 1.8 mm d^{-1} across the models, with typically larger values in atmospheric reanalysis and smaller ones in land surface models (LSMs). Even within the LSM community, considerable disparity exists across different LSMs of the Second Global Soil Wetness Project with a spread reaching ~220 mm yr^{-1} for the global terrestrial ET rate (Schlosser & Gao, 2010). It is therefore necessary and urgent to employ innovative and novel methods for the development of new global ET products with improved accuracy for a better understanding of the terrestrial part of the global hydrological cycle, as advocated by Fisher et al. (2017).

It has long been recognized that the uncertainties in the modeled ET rates are due primarily to uncertainties in the meteorological forcing (Badgley et al., 2015; Vinukollu et al., 2011), model physical structures (Ma et al., 2017;

Zheng et al., 2019) and parameter values (Samaniego et al., 2017; K. Zhang et al., 2019). In particular, the parameter values are often determined by either static or time-varying gridded vegetation (e.g., land cover, leaf-area-index [LAI], canopy height, rooting depth), and soil (e.g., soil type, hydraulic, and thermal properties) data, which are indispensable inputs for most state-of-the-art LSMs (Lawrence et al., 2019) and remote sensing (RS) models (Chen & Liu, 2020) to estimate ET. Numerous sensitivity studies have demonstrated that the accuracy of the latent heat fluxes, as provided by the LSMs and RS models, highly depends on the reliability of the employed soil- and/or vegetation-related parameters (e.g., Cuntz et al., 2016; Dennis & Berbery, 2021; Samaniego et al., 2017). However, formidable challenges in the current global soil data exist, such as (a) gridded soil property characteristics are derived by interpolating field-scale soil survey measurements which then lead to great uncertainties in high-latitude and high-altitude regions where insufficient survey was done (Dai et al., 2019); (b) the empirical functions for deriving gridded hydraulic and thermal parameters from plot-scale soil properties are still struggling with finding the proper extrapolation and upscaling methods from local to global scales (Van Looy et al., 2017), thereby leading to inevitable uncertainties in the modeled ET rates (Dennis & Berbery, 2021). In addition to soil data, the current LAI products, a key input for the Penman-Monteith-type ET models, are neither intra-consistent over time nor inter-consistent with each other (Jiang et al., 2017) due probably to (a) the intrinsic uncertainties in the radiative transfer modeling of light in canopies and the ill-posed inversion problem (Fang et al., 2019), and; (b) sensor degradation or orbital drift (Lyapustin et al., 2014). Last but not least, it is worthwhile to note that most current ET models require precipitation data as forcing, which may greatly facilitate the estimation of ET because accurate precipitation at large spatial and temporal scales may pose an upper bound to constraining terrestrial ET rates (Budyko, 1974), especially in arid and semi-arid regions of the world. However, precipitation is often regarded as the most uncertain meteorological variable due to its high spatial and temporal variance, which may hinder its model forcing value in regions with sparse measurements and/or complex terrain (Clark & Slater, 2006; Lundquist et al., 2019). See Sun et al. (2018) for an exhaustive review on the uncertainties in the current gridded precipitation products.

For circumventing the uncertainties in not only the gridded vegetation and soil data but also in precipitation forcing, the complementary relationship (CR) of evaporation (Bouchet, 1963) naturally presents itself as a suitable choice for large-scale ET estimation because it requires only routine meteorological data as input. Therefore, recently there has been a heightened interest among hydrologists in estimating ET by the CR method across multiple spatial scales, including plot (Crago & Qualls, 2018; Ma, Zhang, Szilagyi, et al., 2015; Ma, Zhang, Xu, et al., 2015), basin (Xu & Singh, 2005), regional (Kyatengerwa et al., 2020; Szilagyi & Jozsa, 2018), and continental one (Ma & Szilagyi, 2019; Szilagyi, 2018). More recently, Brutsaert et al. (2020) presented the first application of the CR method to estimate monthly ET rates (2001–2013) across the globe with a spatial resolution of 0.5°, but they did not fully exploit the unique advantage of the CR of not requiring precipitation forcing, as they parameterized their model with the help of mean annual rain depth values.

Even though the CR can, in general, avoid the uncertainties in gridded soil, vegetation and precipitation forcing by not relying on such input data, the challenge—typical in most diagnostic ET approaches—of how to calibrate the model (Han & Tian, 2020), remains. Calibration is necessary in not only the classical linear CR models (Brutsaert & Stricker, 1979) but also in those recently developed non-linear versions by Brutsaert (2015), Han and Tian (2018), and Gao and Xu (2020), requiring "prior" knowledge of ET (either EC-measured or water-balance-derived) to calibrate a few model parameters, for example, the Priestley–Taylor (PT) coefficient (α). Unfortunately, it is very hard, if not impossible, to obtain appropriate parameter values in poorly gauged and ungauged basins, where limited or missing water-balance (or EC) data make model calibration much more challenging. For the purpose of routinely estimating large-scale ET with the CR, Szilagyi et al. (2017) proposed a novel scheme to derive the PT-α value via temperature and humidity gradients between the wet land and the air obtained by inverting the PT equation (Priestley & Taylor, 1972) over wet grid-cells, the latter automatically identified within a given large spatial domain. In this way, the CR approach no longer requires any ground-truth ET data for the common calibration of its sole parameter, α, thereby overcoming the difficulty in parameter estimation for large-scale ET simulations. The unique calibration-free CR model of Szilagyi et al. (2017) has not yet been applied on a global scale to see whether it is able to improve our understanding of the global terrestrial ET rates, though previous model evaluations suggested that it excels among the current main-stream ET products tested over China (Ma et al., 2019) and the United States (Kim et al., 2019; Ma & Szilagyi, 2019; Ma et al., 2020).

Motivated primarily by large uncertainties existing in the current global ET products reported by numerous studies (e.g., Mueller et al., 2011, 2013; Zeng, Peng, & Piao, 2018), here we extend our previous works on the development of continental-scale ET products (Ma & Szilagyi, 2019; Ma et al., 2019), aiming to provide a new global ET data set by the calibration-free CR method. The objectives are therefore to (a) develop and validate (on multiple spatial and temporal scales) a new global ET product for use in large-scale hydro-climatological research; (b) assess whether this CR-based ET estimation improves upon the available widely used global ET products, and; (c) reveal the spatial characteristics of global terrestrial ET and its tendencies during 1982–2016. This is the first effort of producing a multi-decadal (>30 years with regular planned updates in the future) global ET product by a calibration-free version of the CR method, fully independent of previous LSMs, RS models, atmospheric reanalysis, or machine-learning upscaling of EC measurements, and also, without relying on any vegetation and soil data.

2. Materials and Methods

2.1. The Calibration-Free CR Model

In this study, the calibration-free CR model of Szilagyi et al. (2017) was employed for global-scale terrestrial ET simulation with a brief description of the equations below. For a pseudocode of the calculations, see Appendix C in Ma and Szilagyi (2019). The non-linear CR approach relates two dimensionless evapotranspiration terms via

$$y = \left(2 - X\right)X^2 \tag{1}$$

where X and y are defined as

$$X = \frac{E_{\mathrm{p}}^{\max} - E_{\mathrm{p}}}{E_{\mathrm{p}}^{\max} - E_{\mathrm{w}}}\frac{E_{\mathrm{w}}}{E_{\mathrm{p}}} \tag{2}$$

$$y = \frac{ET}{E_{\mathrm{p}}} \tag{3}$$

here ET (mm d^{-1}) is the actual evapotranspiration rate, while the potential evaporation term, E_{p}, defines the evapotranspiration rate of a small, plot-sized wet patch in a drying (i.e., not fully wet) environment, typically expressed by the Penman (1948) equation as

$$E_{\mathrm{p}} = \frac{\Delta}{\Delta + \gamma}\left(R_{\mathrm{n}} - G\right) + \frac{\gamma}{\Delta + \gamma}f_{\mathrm{u}}\left(e^* - e_{\mathrm{a}}\right) \tag{4}$$

where Δ (kPa $^{\circ}\mathrm{C}^{-1}$) is the slope of the saturation vapor pressure curve at the measured air temperature, T_{a} (°C), and γ is the psychrometric constant (kPa $^{\circ}\mathrm{C}^{-1}$). R_n and G (at the monthly scale the latter can be assumed negligible) are the surface net radiation and soil heat flux into the ground in water equivalent of mm d^{-1}, respectively. e^* and e_{a} (kPa) are the saturation and actual vapor pressure of the air, correspondingly. f_{u} is an empirical wind function (mm d^{-1} kPa^{-1}) that contains the 2-m wind speed, U_2 (m s^{-1}), so that $f_{\mathrm{u}} = 2.6 \times (1 + 0.54 \times U_2)$.

E_{w} in Equation 2 is the wet-environment evaporation rate of a well-watered surface of regional extent, specified by the PT equation (Priestley & Taylor, 1972), that is,

$$E_{\mathrm{w}} = \alpha\frac{\Delta\left(T_{\mathrm{w}}\right)}{\Delta\left(T_{\mathrm{w}}\right) + \gamma}\left(R_{\mathrm{n}} - G\right) \tag{5}$$

in which α is the dimensionless PT coefficient. Note that Equation 5 was derived for completely wet environments (Priestley & Taylor, 1972) and therefore Δ should be evaluated at the air temperature observable in a wet environment, T_{w} (°C), instead of the drying environment air temperature, T_{a} (Szilagyi & Jozsa, 2008). This is important since previous studies have found that the difference between these two may routinely exceed 5°C (e.g., Ma, Zhang, Szilagyi, et al., 2015; Szilagyi, 2014). By making use of a negligible vertical air temperature gradient typically observable in wet environments, T_{w} can be approximated by the wet surface temperature, T_{ws}

(°C). Szilagyi and Schepers (2014) revealed that the wet surface temperature is independent of areal extent, thus T_{ws} can be obtained from the Bowen ratio of a small wet patch for which the Penman equation is valid, that is,

$$\beta_p = \frac{R_n - G - E_p}{E_p} \approx \gamma \frac{T_{ws} - T_a}{e^*\left(T_{ws}\right) - e_a} \tag{6}$$

in which β_p is the Bowen ratio of the well-watered patch (assuming that available energy at the wet patch surface is close to that of the surrounding drying one). The saturation vapor pressure e^* now is evaluated at T_{ws}, substituted for the wet-environment air temperature, T_w. Note that T_{ws} (but not T_w) obtained by Equation 6 may be larger than T_a when the air is close to saturation and in such cases T_{ws} should be capped by T_a (Ma, Zhang, Szilagyi, et al., 2015; Szilagyi, 2014). For large-scale model applications where measured ET is often missing for the calibration of α, the method of Szilagyi et al. (2017) can be employed to assign an appropriate spatially and temporally constant value for it by identifying wet grid-cells with their corresponding gridded T_a and humidity data (see Appendix B in Ma and Szilagyi, 2019 for a detailed explanation of the procedure).

E_p^{max} in Equation 2 is the maximum value that E_p can reach by the time the environment becomes completely desiccated of moisture ($e_a \approx 0$), that is,

$$E_p^{max} = \frac{\Delta\left(T_{dry}\right)}{\Delta\left(T_{dry}\right) + \gamma}\left(R_n - G\right) + \frac{\gamma}{\Delta\left(T_{dry}\right) + \gamma} f_u e^*\left(T_{dry}\right) \tag{7}$$

in which Δ (kPa °C^{-1}) and e^* (kPa) are evaluated at the dry-environment air temperature, T_{dry} (°C). The latter can be estimated for adiabatic processes as (Szilagyi, 2018):

$$T_{dry} = T_{wb} + \frac{e^*\left(T_{wb}\right)}{\gamma} \tag{8}$$

where T_{wb} (°C) is the wet-bulb temperature. T_{wb} under adiabatic conditions can be derived from another iteration (Szilagyi, 2014), that is,

$$\gamma \frac{T_{wb} - T_a}{e^*\left(T_{wb}\right) - e^*\left(T_d\right)} = -1 \tag{9}$$

where T_d (°C) is the dew-point temperature. For a more detailed, thermodynamic-based derivation of Equation 1, see Szilagyi (2021).

2.2. Model Forcing Data

A state-of-the-art meteorological forcing, ERA5 (Hersbach et al., 2020) from the European Center for Medium-Range Weather Forecasts (ECMWF), was employed over the 1982–2016 period globally at a spatial resolution of 0.25° in the form of monthly air and dew-point temperature, air pressure, 10-m wind speed, downward short- and long-wave radiation data. The 10-m wind speed (U_{10}) values were converted to 2-m ones (U_2) by a power-function transformation, that is, $U_2 = U_{10}\,(2/10)^{1/7}$ (Brutsaert, 2005). Being the latest global reanalysis from ECMWF, a wide range of evaluations suggested that the meteorological forcing from ERA5 has an obvious improved accuracy in comparison with previously available global forcing (e.g., Graham et al., 2019; He et al., 2021; Martens et al., 2020), and is therefore appropriate for global ET modeling.

Monthly net radiation (R_n) was calculated by the approach of Ma et al. (2019, Appendix B therein) except that monthly land surface temperature (LST) was now from ERA5-Land rather than from Moderate Resolution Imaging Spectroradiometer (MODIS) because the former could provide a continuous record during the 35-year period of 1982–2016. The albedo (Version 42) and longwave broadband emissivity (Version 40) data came from the Global Land Surface Satellite (GLASS) product (Liang et al., 2021), both produced by the Advanced Very High Resolution Radiometer. The spatial resolution of LST is 0.1°, while albedo and emissivity are at 0.05°, therefore they were resampled to 0.25° to conform with the ERA5 forcing. The monthly radiation-balance-derived grid-values of R_n were further corrected by a multiyear mean monthly coefficient, obtained as the ratio of the radiation-balance-derived multiyear mean monthly R_n and the similar R_n value from the Clouds and the

Earth's Radiant Energy System (CERES) product (Kato et al., 2018) after the latter was also resampled to 0.25°. As CERES is only available since March 2000, here the multiyear mean is taken over their overlap period of 2001–2016. As CERES R_n generally display slight positive biases according to Wild et al. (2015), a constant scaling factor of 0.9186 (Wild et al., 2015) was further applied to the corrected R_n values (except for North America and Europe, because previous validations (Kato et al., 2018) suggested that both, downward short- and long-wave, radiation were underestimated in those regions) for a match with the global terrestrial R_n derived by Wild et al. (2015).

With the final 0.25° R_n as well as the ERA5 T_a, T_d, U_2, and air pressure (the latter for the calculation of γ) data, we derived a spatially and temporally constant PT-α value of 1.10 using the method of Szilagyi et al. (2017), which was then employed for a global terrestrial application of Equations 1–9 over the 1982–2016 period on a monthly basis.

This study focuses only on land surface ET by excluding the sea and inland water bodies as determined by the MODIS land cover type (LCT) product, that is, MCD12C1 Collection 6 (Sulla-Menashe et al., 2019), which also provides the International Geosphere-Biosphere Program (IGBP) based LCT classification. For a proper accounting of the effect of grid resolution on continental areas along the sea shore, the ratio of the continental land area to that of the 0.25° grid—also derived from MCD12C1—was further applied.

2.3. EC-Measured ET Rates From the FLUXNET2015 Database

The monthly eddy-covariance measured latent heat (LE) flux data from the FLUXNET2015 Database (Pastorello et al., 2020) were used to validate the CR simulated results at the plot scale. In the officially released FLUXNET2015 Database, the gaps in the raw half-hourly LE data were filled by the marginal distribution sampling method (Reichstein et al., 2005). Since any gap-filling may involve uncertainties, only the months tagged with "LE_F_MDS_QC" values ≥0.7 (which means that the percentage of measured and good-quality gap-filled data was no less than 70% during the given month) were retained for validation purposes.

EC-site selection was based on the following criteria: (a) the site exists 3 years or longer; (b) surface heterogeneity within the 0.25° cell where the EC tower is situated is minimal, and; (c) at least one third of the monthly LE data released from the FLUXNET2015 Database for this site have "LE_F_MDS_QC" values ≥0.7. As a result, altogether 129 sites (Figure 1a and Table S1) became available for the present study, which include 11 land cover types: cropland (CRO, 14 sites), deciduous broadleaf forest (DBF, 16 sites), deciduous needleleaf forest (DNF, 1 site), evergreen broadleaf forest (EBF, 8 sites), evergreen needleleaf forest (ENF, 27 sites), grassland (GRA, 27 sites), mixed forest (MF, 10 sites), open shrubland (OSH, 3 sites), savanna (SAV, 6 sites), wetland (WET, 12 sites), and woody savanna (WSA, 5 sites). Table S1 presents further information on these 129 sites, while Figure 1a illustrates their spatial distribution.

The number of months for the validations ranges from 13 to 220 among the different sites, yielding a mean data length of 83 months per site (see Table S1 and the inset in Figure 1a). Note that there is only one site (i.e., RU-SkP) within the DNF classification, which was reclassified into the DBF in the assessment of the LCT-specific performance of the model.

For 103 sites, the published LE values are Bowen-ratio corrected (Twine et al., 2000) to satisfy the energy balance closure. For the remaining 26 sites where FLUXNET2015 does not specify the energy-balance-closure-corrected LE values, the measured ones were directly employed for validation.

2.4. Water-Balance-Based Evapotranspiration Data

The modeled ET rates were also validated against the water-balance-derived evapotranspiration (ET_{wb}) values at the basin scale, that is,

$$ET_{wb} = P - Q - \delta S \tag{10}$$

where P, Q, and δS (all three in mm yr^{-1}) are basin-averaged precipitation, runoff, and the change in terrestrial water storage within the basin, respectively. ET_{wb} rates from altogether 52 large river basins (Figure 1b and Table S2) were employed in this study, representing a broad range of climates and land covers. Basin selection

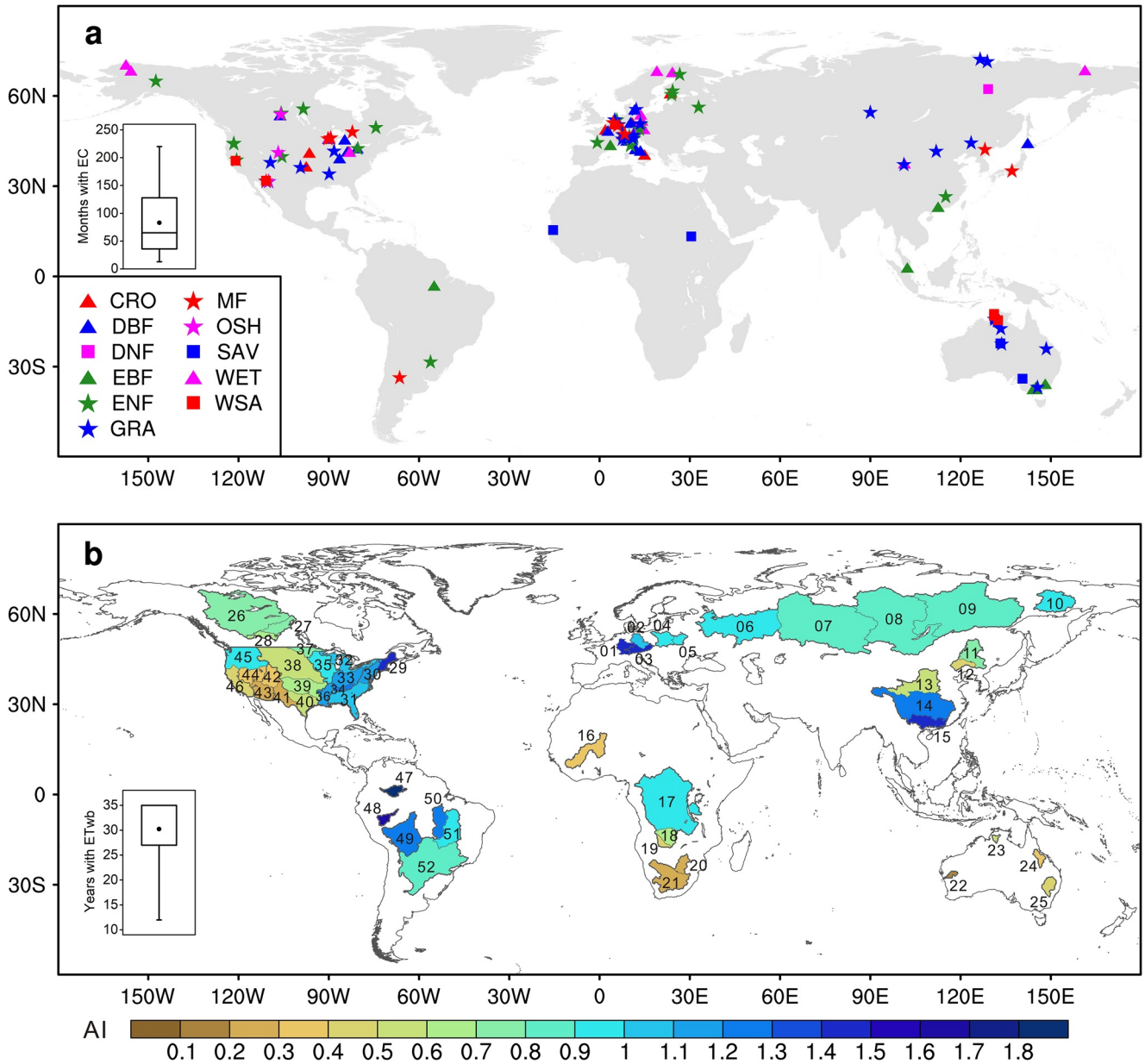

Figure 1. The geographical distribution of the (a) 129 FLUXNET sites, and; (b) 52 river basins for deriving water-balance estimates (ET_{wb}) of basin-wide evapotranspiration. The International Geosphere-Biosphere Program land cover types in (a) include: cropland (CRO), deciduous broadleaf forest (DBF), deciduous needleleaf forest (DBF), evergreen broadleaf forests (EBF), evergreen needleleaf forests (ENF), grassland (GRA), mixed forests (MF), open shrublands (OSH), savannas (SAV), wetland (WET), and woody savanna (WSA). Basin color in (b) denotes the aridity index (AI) defined as the ratio of multi-year mean annual precipitation to Penman potential evapotranspiration. The numbers displayed refer to the basin ID in Table S2. The inset in (a) is the box-plot of months with available eddy-covariance measurements per station for validation of the complementary relationship (CR) model. The inset in (b) is the box-plot of years with ET_{wb} values per basin, employed for validation. Note the same (=35) median and maximum values now. Note also that the whiskers in these two insets represent the minimum and/or maximum values.

was based on (a) basin area is larger than 40,000 km^2 to minimize uncertainties stemming from potential inter-basin water transfer and the relatively coarse spatial resolution of the δS data; (b) a continuous record of at least 12 years (i.e., one third of the present modeling period) of Q data is available to make ET_{wb} accurate in a multiyear mean sense, and; (c) the basins should partially cover all continents except Antarctica where basin-wide precipitation data does not exist. The measured Q values at the hydrological stations for most basins [except those in the conterminous United States (CONUS) and China] came from the Global Runoff Data Center (GRDC), while

Q data of basins in the CONUS and China came from United States Geological Survey (USGS) and the China Sediment Bulletin, respectively.

The drainage area of these 52 basins ranges from 4.7×10^4 to 347.5×10^4 km^2, with mean and median values of 67.3×10^4 and 36.5×10^4 km^2, respectively. The basins are located in tropical, temperate and boreal regions with aridity indices (AI: the ratio of mean annual precipitation to E_p) between 0.13 and 2.44 (Figure 1b). The mean and median AI values of these 52 basins are both 0.85. When a basin did not have a continuous 35-years record of runoff data for 1982–2016, the longest (≥12 years) available such record was used. In the end, a total of 1572 basin-year runoff data were employed to calculate annual ET_{wb} for the validation of the CR-modeled ET rates at the watershed scale. Detailed information about these 52 river basins including name, drainage area, hydrological station, country, continent, and the length of continuous runoff data is presented in Table S2.

For annual P values, the gauge-based precipitation product from the Global Precipitation Climatology Center (GPCC) Full Data Monthly Version 2018 (Schneider et al., 2018) was used except for the CONUS. Over the CONUS, the Parameter-Elevation Regressions on Independent Slopes Model (PRISM) precipitation data (Daly et al., 2008) were employed, because it is regarded as the most accurate precipitation product for that region (Lundquist et al., 2015). Note that PRISM has an overall 4.2-km spatial resolution, thus it was resampled to 0.25° to conform with that of GPCC. While we are aware of another global, gauge-based precipitation product, that is, the Climate Research Unit (CRU) of the University of East Anglia (Harris et al., 2020), the spatial resolution of CRU is 0.5°, which is coarser than that of GPCC (0.25°), plus the latter also fits the resolution of the present CR-modeled ET rates. Furthermore, the GPCC product incorporates roughly three to four times as many precipitation stations as CRU (Becker et al., 2013), thus improving spatial representativeness.

While previous studies suggested that the basin-wide annual δS could be neglected (Brutsaert, 2005), it is more reasonable to consider δS in Equation 10 for a more accurate calculation of ET_{wb} (Han et al., 2020), though it might be a minor term in comparison with P or Q. As the Gravity Recovery and Climate Experiment (GRACE) data is only available since 2002, the 0.5° resolution monthly terrestrial water storage anomaly (TWSA) data from GRACE-REC (Humphrey & Gudmundsson, 2019) were employed in Equation 10. TWSA in GRACE-REC was reconstructed for the past century by a statistical model with inputs of precipitation and temperature at each global terrestrial grid point. GRACE-REC is a state-of-the-art TWSA product consistent with the GRACE data for their temporal overlap. Its century-long coverage including the pre-GRACE period, has made it popular for long-term hydroclimatological studies (Humphrey et al., 2018). The development of GRACE-REC involved two kinds of GRACE products (for training purpose) and three kinds of climate forcing, thus leading to six different versions of it (Humphrey & Gudmundsson, 2019). In the present study, the TWSA version that employed ERA5 precipitation and temperature data as forcing and was calibrated by mascons from the Jet Propulsion Laboratory (JPL) was employed. After re-sampling GRACE-REC into 0.25°, the annual δS values for 1982–2002 were obtained. The annual δS values during 2003–2016 were derived from the JPL Mascon RL06 Version 2.0 GRACE (Watkins et al., 2015) after it was also resampled into 0.25°. Note that the annual δS were calculated as the difference in TWSA between consecutive Decembers.

As the generally strong coupling of the land-atmosphere system weakens considerably near sudden and strong discontinuities in surface moisture status (Morton, 1983), such as found along the sea-shore in desert climates, CR-modeled ET rates were rescaled each month by the ratio of mean annual precipitation and original CR ET values for grid-cells where (a) mean annual precipitation is less than 300 mm; (b) original CR-modeled mean annual ET to precipitation ratio is greater than two, and; (c) the grid cell is within 200 km of the sea (300 km for the Atacama Desert in South America, Western Sahara, and the Horn of Africa). See Figure S1 for the areas involved.

The statistical metrics of assessing the model performance in the present study involve the Pearson correlation coefficient (R), root mean square error (RMSE), relative bias (RB), and Nash-Sutcliffe efficiency (NSE) between modeled results and either EC measurements or water-balance-derived ET_{wb} rates.

2.5. Other Available Global Terrestrial ET Products

For an inter-comparison of the CR ET rates with those of other global ET models, 12 main-stream ET products (Table 1) were selected by the following four categories.

Table 1
Overview of 12 Mainstream ET Products Employed in This study

ET products	Category	Spatial resolution	Spatial coverage	Temporal coverage	References
ERA5	Reanalysis	0.25°	Global land	1982–2016	Hersbach et al. (2020)
MERRA2	Reanalysis	0.5° × 0.625°	Global land without permanent ice and snow	1982–2016	Gelaro et al. (2017)
JRA55	Reanalysis	1.25°	Global land	1982–2016	Kobayashi et al. (2015)
FLUXCOM_WFDEI	Machine learning-based upscaling of EC measurements	0.5°	Global vegetated surface	1982–2013	Jung et al. (2019)
FLUXCOM_GSWP3	Machine learning-based upscaling of EC measurements	0.5°	Global vegetated surface	1982–2014	Jung et al. (2019)
FLUXCOM_CRUNCEP	Machine learning-based upscaling of EC measurements	0.5°	Global vegetated surface	1982–2016	Jung et al. (2019)
Noah_GL	Land surface model	0.25°	Global land without Antarctic	1982–2014	Beaudoing and Rodell (2019)
CLSM_GL	Land surface model	1°	Global land without Antarctic	1982–2014	Li et al. (2019)
VIC_GL	Land surface model	1°	Global land without Antarctic	1982–2014	Beaudoing and Rodell (2020)
GLEAM	Remote sensing model	0.25°	Global land	1982–2016	Martens et al. (2017)
PLSH	Remote sensing model	0.0833°	Global land without permanent ice and snow	1982–2013	K. Zhang et al. (2015)
PML_V2	Remote sensing model	500 m	Global land without permanent ice and snow	2003–2016	Y. Zhang et al. (2019)

Note. The periods of temporal coverage displayed are the overlaps with that of the CR (i.e., 1982–2016).

Abbreviations: CR, complementary relationship; CRUNCEP, Climate Research Unit and National Centers for Environmental Prediction; EC, eddy-covariance; ET, evapotranspiration; JRA, Japanese reanalysis; GLEAM, Global Land Evaporation Amsterdam Model; GSWP, Global Soil Wetness Project; MERRA, Modern-Era Retrospective Analysis for Research and Applications; PLSH, Process-based Land Surface Evapotranspiration/Heat Fluxes Algorithm; PML, Penman-Monteith-Leuning; WFDEI, WATCH Forcing Data ERA-Interim.

1. Three atmospheric reanalysis ET products from the ERA5 of ECMWF (Hersbach et al., 2020), the Modern-Era Retrospective Analysis for Research and Applications Version 2 (MERRA2) of NASA's Global Modeling and Assimilation Office (Gelaro et al., 2017), and the Japanese 55-years reanalysis (JRA55) of the Japan Meteorological Agency (Kobayashi et al., 2015). It should be noted that the ERA5's ET estimation is based on its land surface model, called Hydrology Tiled ECMWF Scheme for Surface Exchanges over Land (Hersbach et al., 2020), which is totally different from the present CR method, though both employ ERA5 meteorological data as forcing.
2. Three state-of-the-art machine learning-based upscaling of EC measurements from FLUXCOM (Jung et al., 2019), which were driven by remote sensing data plus different meteorological forcing (i.e., RS_METEO) including (a) WATCH Forcing Data ERA-Interim (WFDEI; Weedon et al., 2015); (b) Global Soil Wetness Project 3 Forcing (GSWP3; Kim, 2017), and; (c) a fused forcing of the Climate Research Unit and National Centers for Environmental Prediction (CRUNCEP; Wei et al., 2014).
3. Three LSM-based ET products from the Global Land Data Assimilation System version 2.0 (GLDAS-2; Rodell et al., 2004), which includes Noah_GL (Beaudoing & Rodell, 2019), CLSM_GL (Li et al., 2019), and VIC_GL (Beaudoing & Rodell, 2020).
4. Three RS-based ET products from the Global Land Evaporation Amsterdam Model (GLEAM) Version 3.3a (Martens et al., 2017), the Process-based Land Surface Evapotranspiration/Heat Fluxes Algorithm (PLSH; K. Zhang et al., 2015), and the Penman-Monteith-Leuning Version 2 (PML_V2; Y. Zhang et al., 2019).

The period of comparison was restricted to the temporal coverage of the present CR ET values, that is, 1982–2016, or to their overlap with it. Note that the spatial coverage may be different among the models as desert and/or permanent snow and ice (e.g., Antarctica and Greenland) areas may be excluded in certain ET products. From these 12 products, only ERA5, JRA55, and GLEAM cover the global land surface fully. Table 1 displays additional information about the products, while full details can be found in the references specified therein.

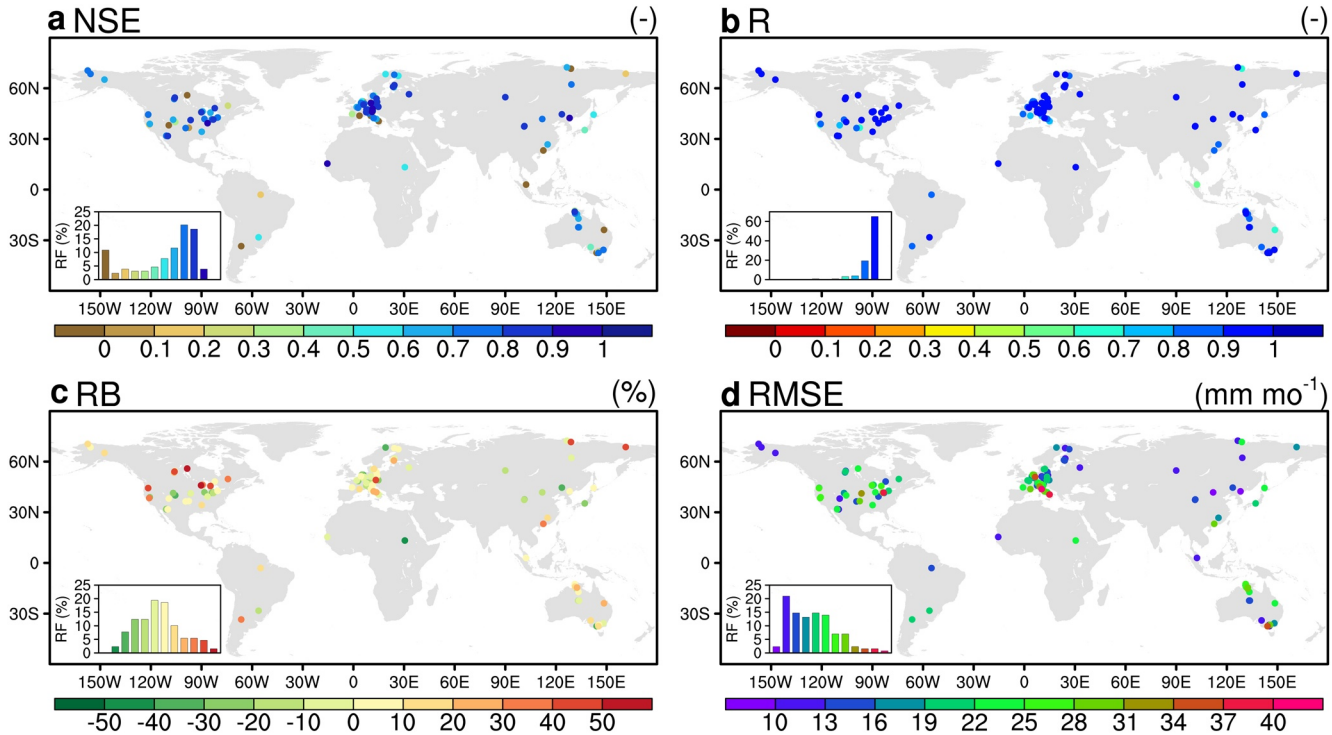

Figure 2. Spatial distribution of the statistical metrics including (a) Nash-Sutcliffe efficiency (NSE); (b) Pearson correlation coefficient (R); (c) relative bias (RB), and; (d) root-mean-square-error (RMSE) for validating the monthly complementary relationship (CR)-simulated evapotranspiration rates against eddy-covariance-measured results of the 129 FLUXNET sites. The inset in each panel displays the histogram of relative frequency (RF) of the performance values with bin limits (and matching color) specified in the horizontal bars.

In addition to the above main-stream ET products, outputs from the "historical simulation" of 20 Earth System Models that participated in the Coupled Model Inter-comparison Project Phase 6 (CMIP6; Eyring et al., 2016) were also included for further comparison. The CMIP6 historical experiments, driven by historical all/individual forcing, were designed to simulate a wide range of variables in the climate system from 1850 to 2014 with a consideration of numerous observed records (representing impacts from both human activities and natural variations) including greenhouse gas emissions and land use changes. While a great number of models participated in the CMIP6 project, we selected only those 20 that yielded the longest overlap with the CR ET data in this study (i.e., 1982–2014 vs. 1982–2016). Note that the present selection of CMIP6 models was mostly based on the "one institute, one model" criterion, though it may be somewhat arbitrary. For each model, the ensemble member "r1i1p1" was used. Further information about the selected CMIP6 models can be found in Table S3.

Since there are differences in the spatial resolution of the above ET datasets (see Tables 1 and S3), all ET products were first resampled into 0.25° by the nearest neighbor method, followed by calculation of the area-weighted ET rates for each river basin. Similar spatial averages were also obtained for the global land area and for the vegetated surface only, again, with consideration of the land fraction in each 0.25° grid along the sea shore. The least squares regression technique was used to estimate the trend in annual ET values. The statistical significance of the trend was determined using the Student's *t* test and a trend is considered to be statistically significant when the *p* value is smaller than 0.05.

3. Results

3.1. Validation Against Plot-Scale Monthly FLUXNET EC Measurements

Figure 2 illustrates the spatial distribution of the statistical metrics for validating the CR estimated monthly ET rates against 129 EC sites from the FLUXNET2015 Database. Albeit about 10% of the sites display negative NSE values, the same values are larger than 0.5 in more than 72% of the stations, suggesting that the modeled results are satisfactory in the majority of the FLUXNET sites (Figure 2a). Furthermore, 61 sites have NSE values

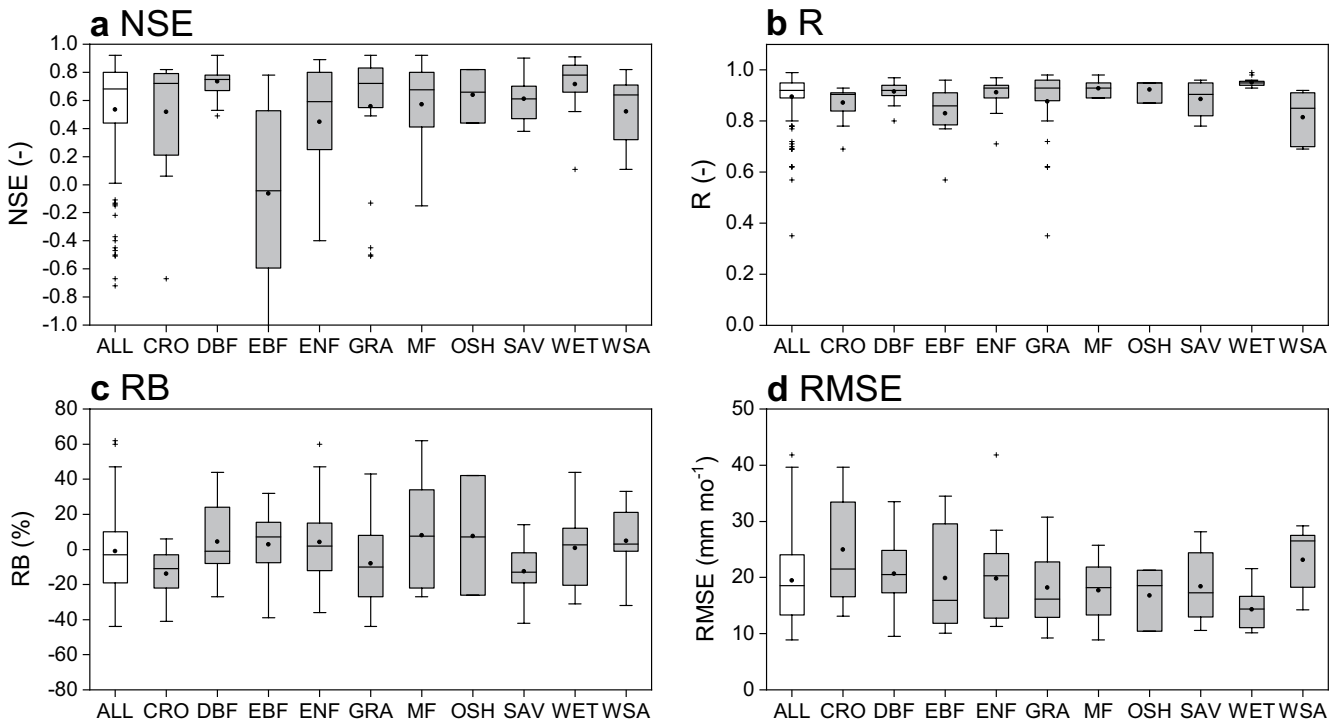

Figure 3. Box plots of the statistical metrics for validating the complementary relationship (CR)-simulated evapotranspiration rates against eddy-covariance-measured results of all 129 FLUXNET sites (ALL) and the sites grouped by land cover type. On each box, the central line is the median (t_2), while the edges of the box are the 25th (t_1) and 75th (t_3) percentiles, respectively. The whiskers extend to the most extreme data points [t_3+1.5 × (t_3−t_1)] and [t_1−1.5 × (t_3−t_1)] not considered outliers, while the outliers are plotted individually using crosses. The filled point is the mean value.

in excess of 0.7. The simulated monthly ET rates correlate highly with measurements due to the inherent seasonality in ET. The R values are larger than 0.8 in about 88% of the selected sites, with 89 sites having R values in excess of 0.9 (Figure 2b). For the relative bias, 40% of the total sites are within ±10%, while 60% have an RB within ±20% (Figure 2c). The RMSE values are smaller than 30 mm mo^{-1} at approximately 90% of the 129 sites (Figure 2d).

Figure 3 summarizes the performance of CR for each LCT. Averaged over the 129 sites, the mean and median NSE values are 0.53 and 0.68, respectively. The median NSE stays between 0.59 and 0.78 for nine LCTs (Figure 3a). However, four EBF sites show even negative NSE values. The R values are overall high with median values larger than 0.85 for all LCTs (Figure 3b). In terms of RB, negative biases dominate in GRA, SAV, and CRO, while positive biases occur more frequently for sites within DBF, EBF, and MF (Figure 3c). While the ET rates vary greatly across different LCTs, the median RMSE value stays below 20 mm mo^{-1} for the majority of the LCTs. For all 129 sites, the mean and median of RMSE are 19.5 and 18.5 mm mo^{-1}, respectively (Figure 3d). Overall, the multi-biome validations against the FLUXNET2015 Database suggest that the CR model performance is satisfactory in a wide range of terrestrial ecosystems with diverse climates across the world even though (a) the PT-α value was derived without resorting to any (EC-measured or water-balance-derived) ET data; (b) there are large differences in the spatial representativeness of the 0.25° grid employed and the footprint of EC measurements, and; (c) the CR was driven by global reanalysis-based meteorological forcing rather than the measured ones from EC towers.

To further illustrate how the CR performs in different LCTs in comparison with other ET products, the median values of the four statistical metrics are also displayed in Figure S2 for the 12 mainstream ET products of Table 1. As seen, the performance of the different ET products varied significantly across the LCTs. No single ET product could perform best for all land covers, including the FLUXCOM versions which were upscaled from these EC towers. In general, the CR performs better (notice the location of the black horizontal line over each LCT) than most ET products for the majority of land covers except EBF. The relatively poor performance of the CR in EBF remains unclear, but ERA5 ET rates also yield a similarly low NSE value there (Figure S2a), indicating

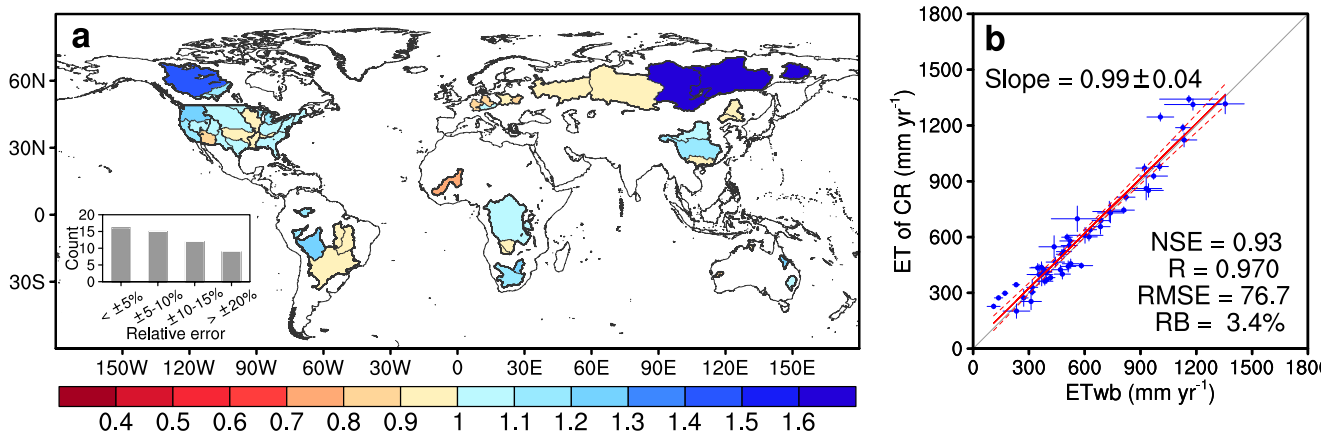

Figure 4. (a) Spatial distribution of the basin-averaged multi-year mean annual complementary relationship (CR) evapotranspiration (ET) rates relative to the ET_{wb} of the 52 river basins, and; (b) the corresponding regression plot. Period of averaging follows that of the corresponding ET_{wb}. The inset in panel (a) shows the number of basins with the specified relative error ranges. The length of the whiskers in panel (b) represents the standard deviation of the annual values of each basin. The strips around the least-squares-fitted red line with its slope specified denote the 95% confidence intervals. The root-mean-square-error (RMSE) is in mm yr^{-1}.

that uncertainties in the ERA5 meteorological forcing may be responsible for their mutually poor performance in EBF.

3.2. Validation Against Basin-Scale Multiyear Mean ET_{wb}

The water-balance-derived multiyear mean annual ET_{wb} rates of the 52 large river basins of the present study (Figure 4) suggest that the CR modeled such ET rates are particularly accurate: NSE = 0.93, R = 0.970, and RB = 3.4%, with a slope of regression almost identical to unity, and RMSE of only 76.7 mm yr^{-1} (Figure 4b). The relative errors are within ±10% for 31 basins out of the 52 (see the inset in Figure 4a). However, the CR overestimates ET_{wb} by more than 60% over three Arctic basins in eastern Siberia including Yenisy (Basin #08), Lena (Basin #09), and Kolyma (Basin #10), while underestimates it by 23% over the Niger River basin (Basin #16) in West Africa. Such relatively larger errors in these basins may be attributed to accuracy issues in the gridded model forcing because the ground meteorological stations that were assimilated into the ERA5 reanalysis are much sparser in the sub-Sahara and the sub-Arctic than in other regions of the world. Another source of uncertainty in the ET_{wb} values may also stem from the limited number of precipitation stations included in GPCC for these regions, leading to uncertain basin-wide P values.

Overall, the CR model's performance with the current meteorological forcing, primarily from ERA5, is comparable with earlier country-scale results driven by PRISM and North American Regional Reanalysis (NARR) forcing over the CONUS (Ma & Szilagyi, 2019) as well as the China Meteorological Forcing Data set over China (Ma et al., 2019).

For a comparison against other mainstream approaches, Figure 5 displays the validation results of the 12 selected ET products against ET_{wb} in a multiyear mean annual sense. Note that for each basin, the multiyear mean values of ET are specified for the period-overlap between ET_{wb} and the corresponding ET product. It can be seen that FLUXCOM_GSWP3 yields the highest NSE (0.91) and the lowest RMSE (88.7 mm yr^{-1}) values among the 12 products (Figure 5e), followed closely by Noah_GL (Figure 5g) and PML_V2 (Figure 5l) with similar NSE (0.9 and 0.89, respectively) and RMSE (93.7 and 94.5 mm yr^{-1}, respectively) values. These latter two yield better RB values (3.1% and 4.5%, respectively) than FLUXCOM_GSWP3 (7.3%). FLUXCOM_WFDEI, PLSH, and ERA5 are also satisfactory, as can be seen from their NSE values in excess of 0.85 (Figures 5a, 5d and 5k). VIC_GL significantly underestimates ET in most basins with NSE = 0.41, RMSE = 228.4 mm yr^{-1}, and RB = −32.5%, while MERRA2 shows large positive biases over the majority of basins with an RB value of 22.3%.

By comparing the performance metrics in Figures 4b and 5 as well as Table 2, it can be stated that the current CR approach excels among the main-stream ET products in its regression slope, NSE, and RMSE values. Noah_GL produces the lowest RB value, while ERA5, FLUXCOM_WFDEI, and CR yield the highest R values (all around 0.97).

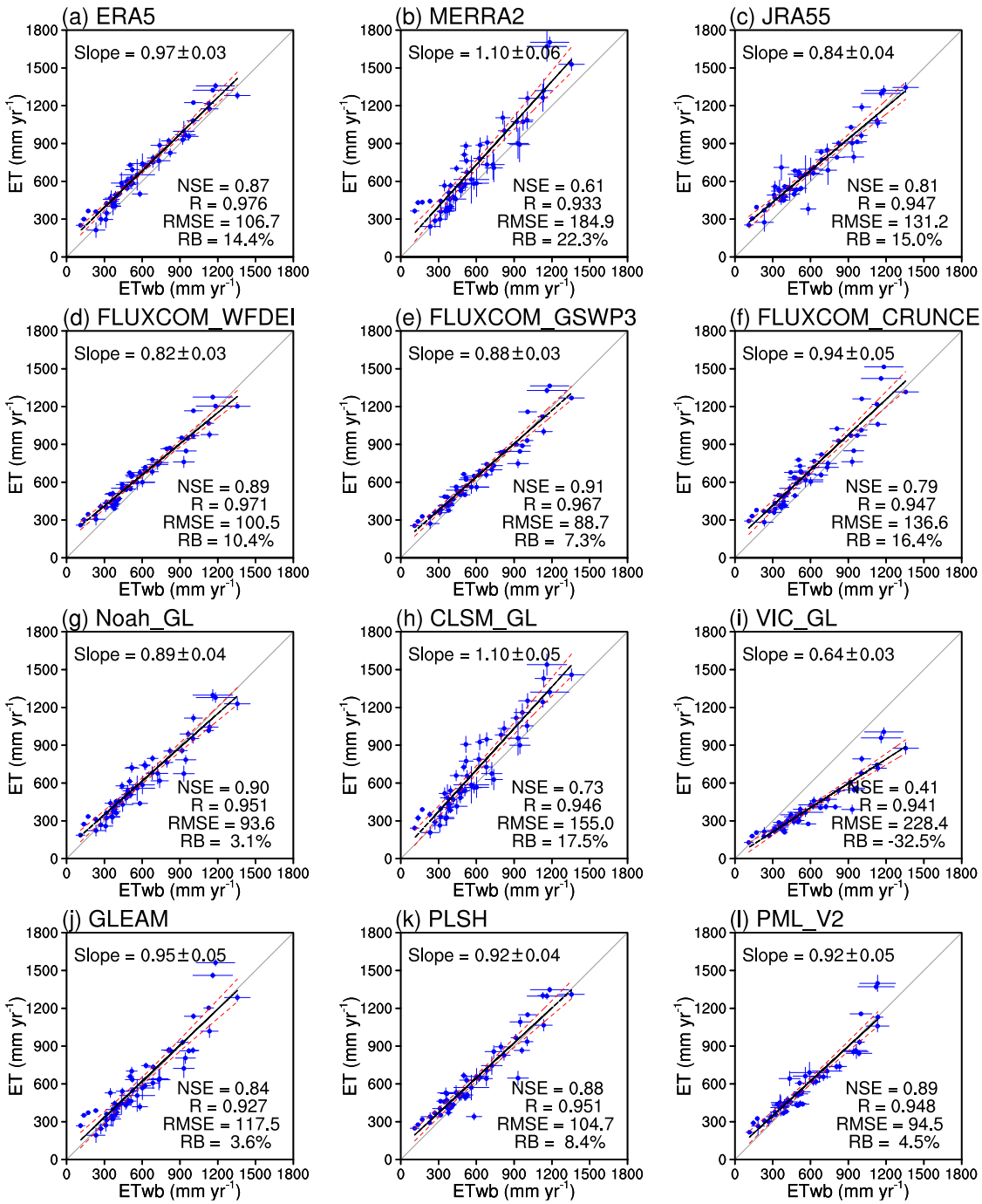

Figure 5. Regression plots of the basin-averaged multi-year mean annual evapotranspiration (ET) rates from the 12 ET products against ET_{wb} of the 52 river basins. Averaging period follows the overlapping temporal coverage of the corresponding ET product and the ET_{wb}. The length of the whiskers represents the standard deviation of the annual values in each basin. The strips around the least-squares-fitted red line with the slope specified denote the 95% confidence interval. The root-mean-square-error (RMSE) is in mm yr^{-1}.

The spatial patterns of the ratio of basin-averaged multiyear mean ET to ET_{wb} over the 52 basins are illustrated in Figure 6 for the 12 ET products. Note that validations of PML_V2 were made for only 49 basins as the remaining three have no ET_{wb} data before 2003. As seen, three atmospheric reanalysis products (ERA5, MERRA2, and JRA55; Figures 6a–6c) and FLUXCOM_CRUNCEP (Figure 6f) tend to overestimate ET in most basins, while VIC_GL (Figure 6i) performs oppositely with substantial negative biases. In addition to VIC_GL, a remarkable underestimation of ET in the Niger River basin also occur in PLSH (−41%), GLEAM (−28%), Noah_GL

Table 2
Performance Statistics of the CR and the 12 Mainstream ET Products Over 52 River Basins of the Globe

		Multiyear mean annual ET					Annual ET				
Models	Period	Slope (−)	R (−)	RMSE (mm yr^{-1})	RB (%)	NSE (−)	Slope (−)	R (−)	RMSE (mm yr^{-1})	RB (%)	NSE (−)
CR	1982–2016	**0.99**	0.970	**76.7**	**3.4**	**0.93**	0.93	0.952	**88.3**	6.2	**0.88**
ERA5	1982–2016	0.97	**0.976**	106.7	14.4	0.87	0.93	**0.957**	117.1	18.0	0.80
MERRA2	1982–2016	1.10	0.933	184.9	22.3	0.61	**1.03**	0.901	189.5	28.8	0.47
JRA55	1982–2016	0.84	0.947	131.2	15.0	0.81	0.80	0.922	145.4	18.4	0.71
GLEAM	1982–2016	0.95	0.927	117.5	3.6	0.84	0.89	0.907	122.7	**3.8**	0.81
FLUXCOM_CRUNCEP	1982–2016	0.94	0.947	136.6	16.4	0.79	0.88	0.926	143.7	21.6	0.70
CR	1982–2014	**0.99**	**0.970**	**76.9**	3.6	**0.93**	0.93	**0.953**	**88.9**	6.2	**0.88**
FLUXCOM_GSWP3	1982–2014	0.88	0.967	88.7	7.3	0.91	0.83	0.950	101.2	12.0	0.85
Noah_GL	1982–2014	0.89	0.951	93.7	**3.1**	0.90	0.86	0.931	106.4	**5.6**	0.85
CLSM_GL	1982–2014	1.10	0.946	155.0	17.5	0.73	**1.04**	0.919	161.7	17.8	0.70
VIC_GL	1982–2014	0.64	0.941	228.4	−32.5	0.41	0.60	0.923	226.0	−32.4	0.37
CR	1982–2013	**0.99**	0.970	**77.3**	**3.8**	**0.93**	**0.93**	0.953	**89.3**	**6.2**	**0.88**
FLUXCOM_WFDEI	1982–2013	0.82	**0.971**	100.5	10.4	0.89	0.79	**0.957**	111.9	16.3	0.80
PLSH	1982–2013	0.92	0.951	104.7	8.4	0.88	0.88	0.933	114.5	8.3	0.79
CR	2003–2016	**1.00**	**0.962**	**82.8**	**4.0**	**0.91**	**0.92**	**0.945**	**88.5**	11.6	**0.86**
PML_V2	2003–2016	0.92	0.948	94.5	4.5	0.89	0.84	0.931	98.8	**8.1**	0.85

Note. Outstanding values in each category and model period (separated by horizontal lines) are in bold.

Abbreviations: CR, complementary relationship; CRUNCEP, Climate Research Unit and National Centers for Environmental Prediction; ET, evapotranspiration; JRA, Japanese reanalysis; GLEAM, Global Land Evaporation Amsterdam Model; GSWP, Global Soil Wetness Project; MERRA, Modern-Era Retrospective Analysis for Research and Applications; NSE, Nash-Sutcliffe efficiency; PLSH, Process-based Land Surface Evapotranspiration/Heat Fluxes Algorithm; PML, Penman-Monteith-Leuning; R, correlation coefficient; RMSE, root mean square error; RB, relative bias; WFDEI, WATCH Forcing Data ERA-Interim.

(−25%), and JRA55 (−35%), which is consistent with the performance of the CR in the same basin. It is also evident that all 12 products, similar to the CR, significantly overestimate ET over the three Arctic basins (i.e., Yenisy, Lena, and Kolyma) in eastern Siberia for reasons discussed above.

3.3. Validation Against Basin-Scale Annual ET_{wb}

Figure 7 presents the validation of the CR-simulated annual ET rates (1982–2016) against 1572 basin-year annual ET_{wb} values of Equation 10. In comparison with the statistical metrics in Section 3.2, the performance of the CR deteriorates slightly with NSE = 0.88, RMSE = 88.3 mm yr^{-1}, RB = 6.2%, and best-fit-line slope of 0.93. This is so because the current metrics come from temporal statistics of annual values from all 52 basins at once, while the same metrics in the previous multiyear mean sense represent spatial statistics (of the basin multiyear averages). In other words, spatial statistics may be perfect as long as the model is unbiased for each basin even when the annual predictions show absolutely no correlation with "measurements."

Owing to the same reason, the statistical metrics also degrade for the 12 ET products on an annual basis (Figure S3 and Table 2). Note again that for each basin the validations of the models' annual ET rates were performed only for the overlap period with ET_{wb}, thus the sample size may vary by ET products in Figure S3. With annual values, FLUXCOM_GSWP3, Noah_GL, and PML_V2 continue to produce the highest NSE (all are 0.85) and lowest RMSE (~100 mm yr^{-1}) values. This is followed by GLEAM, ERA5, FLUXCOM_WFDEI, and PLSH, with NSE values around 0.80 and RMSE about 110–120 mm yr^{-1}. Similar to the multiyear mean case, VIC_GL, and MERRA2 again exhibit the largest errors with NSE <0.5 and RMSE >180 mm yr^{-1}.

For a better inter-comparison, the CR-simulated ET rates were again assessed for the different time-periods of the ET products (see Figures S3m–S3o and Table 2). It can be seen that the CR's NSE and RMSE values excel independent of the temporal coverage. ERA5 and FLUXCOM_WFDEI reach an R value (both 0.957) which is

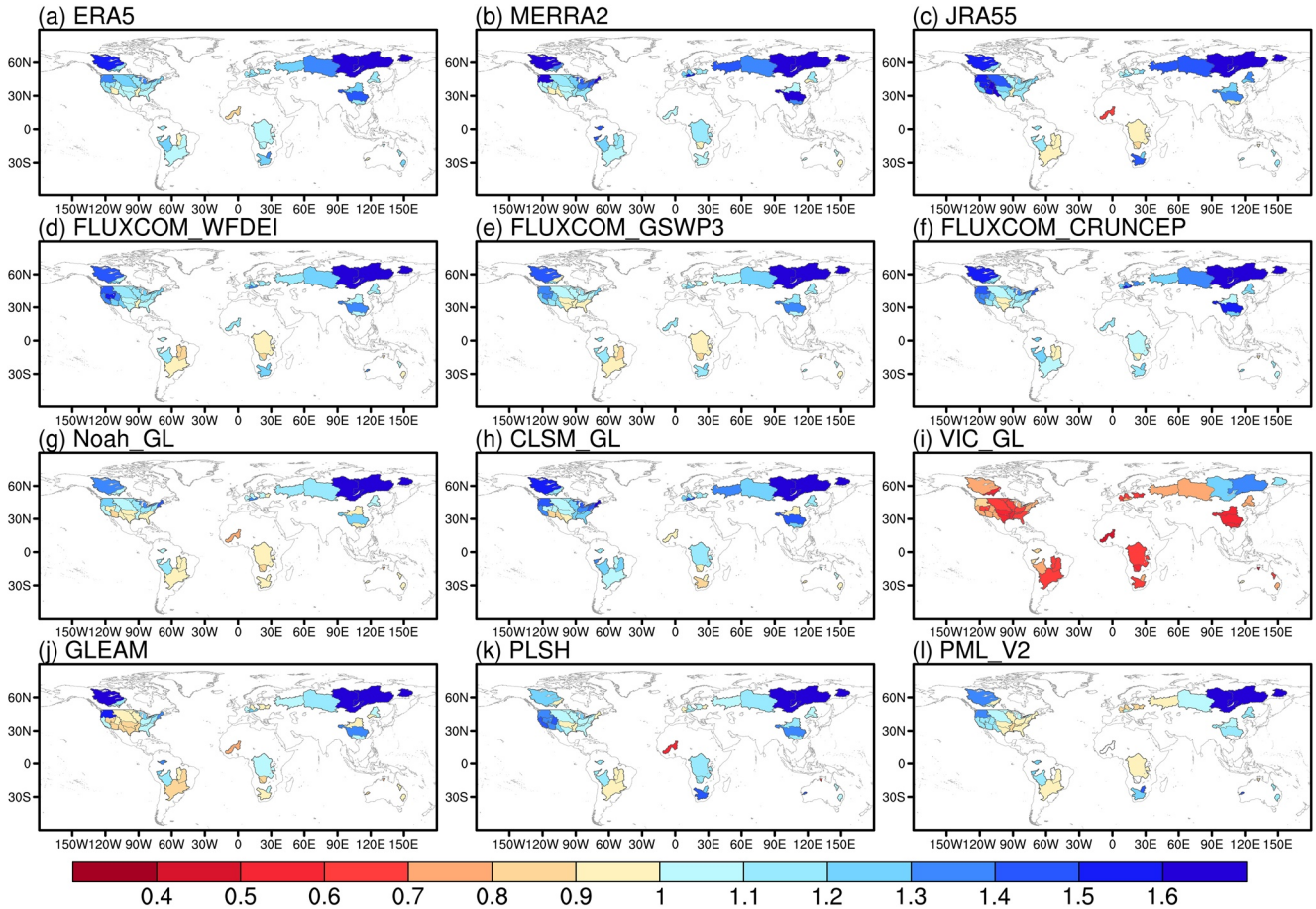

Figure 6. Spatial distribution of the basin-averaged multi-year mean annual evapotranspiration (ET) rates from the 12 mainstream ET products relative to the ET_{wb} of the 52 river basins. Averaging period follows the overlapping temporal coverage of the corresponding ET product and the ET_{wb}.

practically the same as that of the CR (0.952 and 0.953). Only MERRA2 and CLSM_GL have better regression-line slope values than the CR, while GLEAM, Noah_GL, and PML_V2 yield smaller RB values than the CR.

In general, the annual validations against ET_{wb} confirm again that the CR generally improves upon (or at least it is on a par with) the selected main-stream ET products in its performance metrics discussed.

3.4. Spatial Variations in Global ET Rates

Figure 8 displays the global (and latitudinal) distribution of the multiyear (1982–2016) mean annual ET rates simulated by the CR. It can be seen that ET rates are high in the tropical regions (Amazon/Congo basins, and Southeast Asia) around the equator with values often exceeding 1200 mm yr^{-1}, while intermediate ET rates occur in the mid-latitude forests and agricultural regions. Beside the permanently ice and snow-covered regions of Antarctica and Greenland, low ET rates occur in the arid regions of the continents (e.g., Sahara, Central Asia, southwestern United States), and the boreal (e.g., Northern Siberia and Northern Canada) regions of the world with values mostly below 200 mm yr^{-1}. In general, the spatial pattern of the annual ET rates and the latitudinal-averages from the CR are all consistent with those from the ensemble means of the main-stream ET products as well as the 20 CMIP6 models, as have been illustrated in Figure S4.

The multiyear mean annual global land ET rate from the CR is 500 ± 6 (mean ± standard deviation) mm yr^{-1}, which equals to 72.3 ± 0.9 × 10^3 km^3 yr^{-1} for the total amount. This indicates that the annually evaporated water volume from the global land surface is about triple (~3.2) the total water volume of the Great Lakes (22.8 × 10^3 km^3 according to NOAA Great Lakes Environmental Research Laboratory at https://www.glerl.noaa.

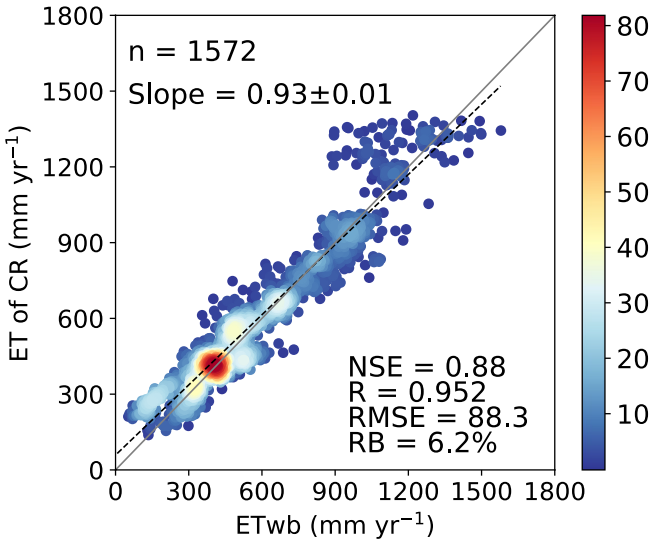

Figure 7. Regression plots of the basin-averaged annual complementary relationship (CR) evapotranspiration (ET) rates against ET_{wb} of the 52 river basins (1982–2016). For each basin, comparisons were possible only for years with annual ET_{wb} available, yielding a total sample size (n) of 1572. The annual ET rates were binned first with a bin-length of 50 mm, followed by a 2-D spline-smoother of the bin counts (vertical bar). The statistical metrics displayed are for the original annual values. The root-mean-square-error (RMSE) is in mm yr^{-1} and the least-squares-fitted (dashed) line is also displayed.

gov/education/ourlakes/lakes.html). This annual volume is also close to that stored in the Caspian Sea (78.2×10^3 km^3), the largest inland water body on Earth in terms of area and volume.

Figure 9 compares the multiyear (for the common overlap period of 1982–2013 for all models except PML_V2 with its original time-period kept) mean annual global land- and vegetated-surface ET rate among the models. See Figure S5 for the vegetated surface domain and Table 1 for the spatial coverage of each product. For the global land-averaged ET rate, the CR yields a somewhat larger value than GLEAM, but both are much smaller than those of the two reanalysis products, that is, ERA5 and JRA55 (Figure 9a). For the global vegetated surface-averaged ET rate, the CR ranks fifth (in increasing order) among them. Such an ET rate of the CR is very close to those of FLUXCOM_GSWP3, PLSH, and PML_V2, the first one equaling the median of these 13 products. The largest two ET rates in Figure 9a come from FLUXCOM_CRUNCEP and MERRA2 (both in excess of 670 mm yr^{-1}), both exhibiting obvious overestimations in Figures 5b and 5f; while VIC_GL, which significantly underestimates ET in Figure 5i, produces an unreasonably low value of 365 mm yr^{-1} for the global vegetated surface (Figure 9a).

In comparison with the 20 CMIP6 models, CR ranks eighth (in increasing order) for both global land- and vegetated-surface ET rates (Figure 9b). In general, not only the median and mean global land ET rates of CMIP6 but also their inter-model spread is larger than those from the other 13 ET products (compare the box-plots of Figures 9a and 9b).

3.5. Continental and Land-Cover-Type ET Rates

Among the CR's continent-averaged values (Figure 10a and Table S4), the largest multiyear (1982–2016) mean annual ET rate occurs over South America with a value of 1023 ± 12 mm yr^{-1}, which is almost twice the second largest value for Africa (565 ± 10 mm yr^{-1}). With the exception of Antarctica where ET rates are, as expected,

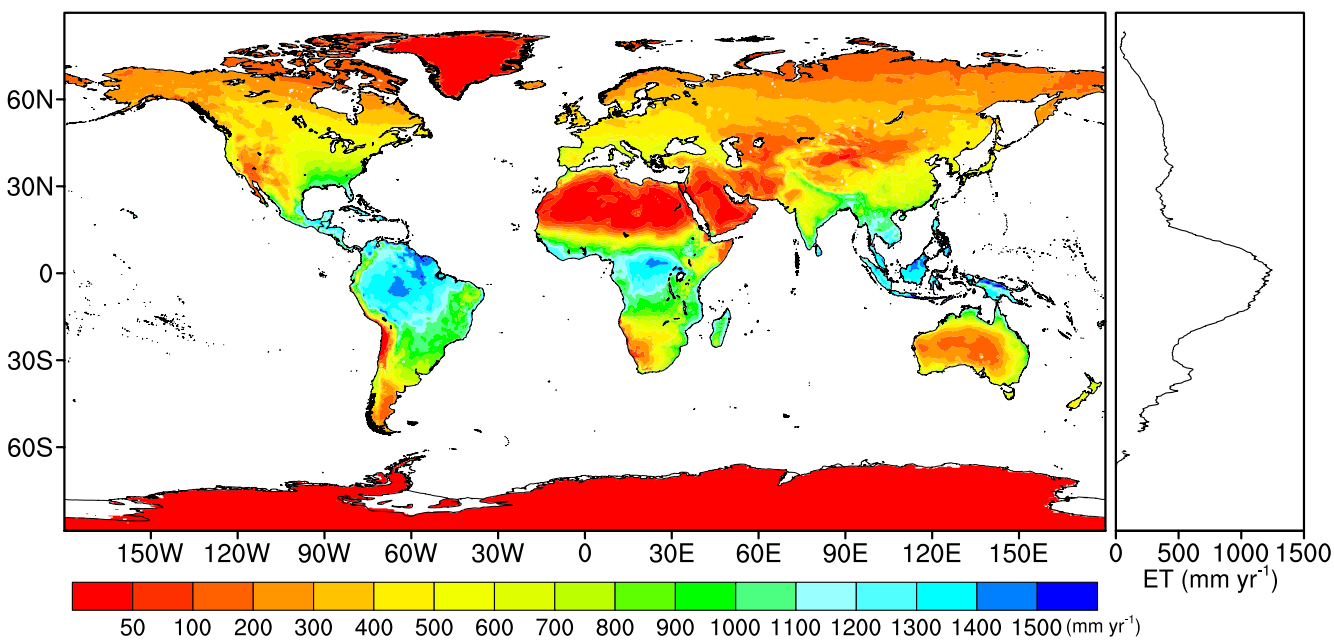

Figure 8. Spatial pattern of the complementary relationship (CR)-modeled multiyear mean (1982–2016) annual terrestrial evapotranspiration (ET) rates across the globe and their latitudinal-averages.

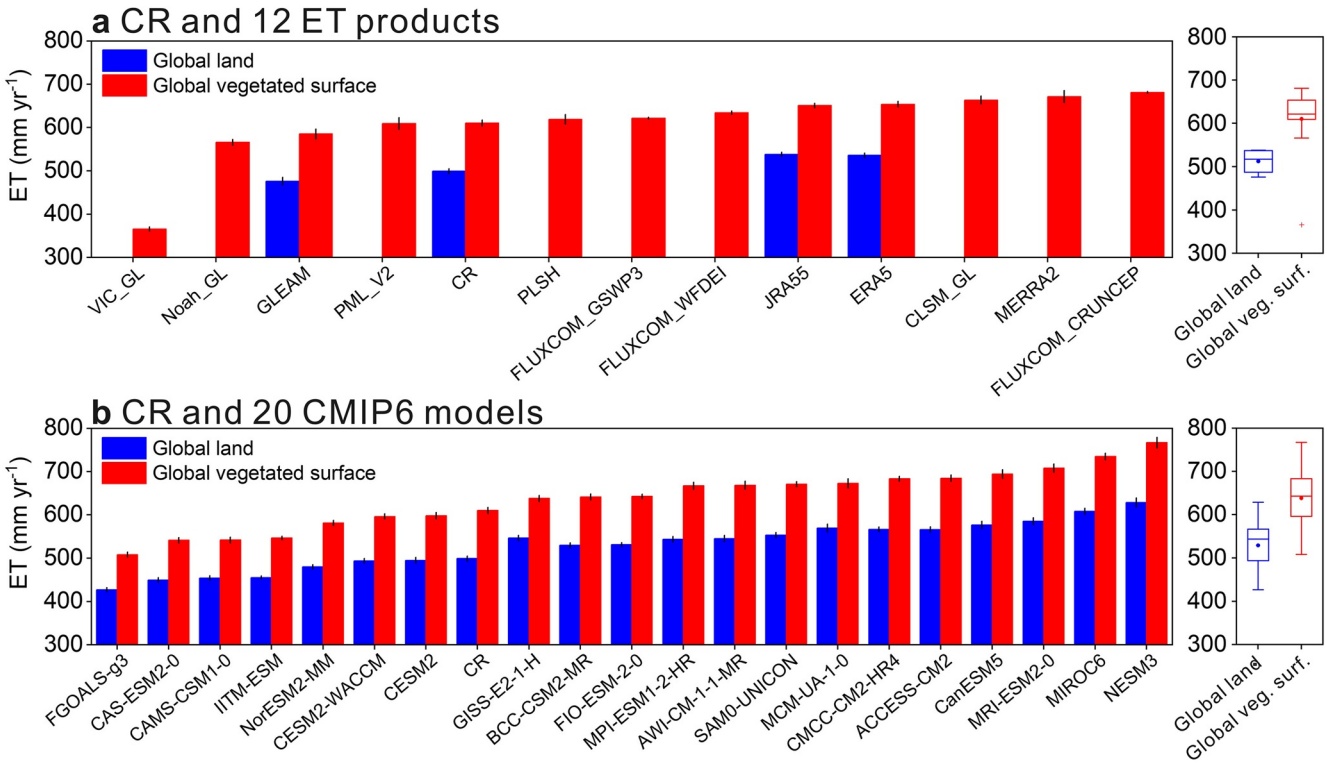

Figure 9. Comparison of the multi-year mean annual complementary relationship (CR) evapotranspiration (ET) estimate against those of (a) the 12 mainstream ET products, and; (b) 20 Coupled Model Inter-comparison Project Phase 6 (CMIP6) models for the global land and the global vegetated surface only. Averaging period is the 1982–2013 overlap for all models except PML_V2 (2003–2016). The error bar represents inter-annual variability of the modeled values. For each group's box plot, the central line is the median, while the edges of the box are the 25th and 75th percentiles, respectively. The whiskers extend to the most extreme data points without considering outliers, while the outlier marked individually by a plus sign. The filled point is the mean value.

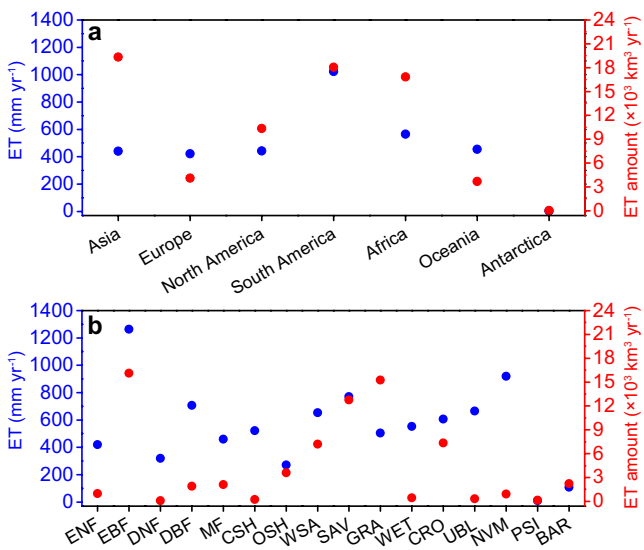

Figure 10. Multiyear (1982–2016) mean annual evapotranspiration (ET) rates and the corresponding ET amount modeled by the complementary relationship (CR) for each (a) continent and (b) International Geosphere-Biosphere Program (IGBP) land cover type.

particularly low, the other four continents exhibit similar annual ET rates ranging from 420 to 460 mm yr^{-1} (Table S4). However, because of large differences in continental areas, the largest absolute ET amount is found over Asia with a value of 19.3 ± 0.4 × 10^3 km^3 yr^{-1}, followed by South America (18.0 ± 0.2 × 10^3 km^3 yr^{-1}), and Africa (16.8 ± 0.3 × 10^3 km^3 yr^{-1}). These three continents contribute ~75% of the total water evaporated from the global land surface, though their total area only accounts for ~54% of the global land area. In general, the ET amounts estimated by the CR over the continents are comparable to previous results documented by Rodell et al. (2015, Figure 3 therein) and Jung et al. (2019, Figure 8 therein).

Among the IGBP land cover types (Figure 10b and Table S4), evergreen broadleaf forests (EBF), mostly of the tropics (see Figure S6 for the full name and spatial distribution of each LCT), produce both the largest annual ET rate (1263 mm yr^{-1}) and the largest total amount of ET (16.1 × 10^3 km^3 yr^{-1}), whereas permanent snow and ice (PSI) and barren land (BAR) do the smallest, which together contribute ~3% to the total global terrestrial ET amount. Although the annual ET rate from grasslands (GRA) is only about 500 mm yr^{-1}, the relatively large area of such a LCT makes it the second largest contributor (~21%) to the total amount of global terrestrial ET with a value of 15.2 × 10^3 km^3 yr^{-1}, which is slightly higher than the third largest contributor, savannas (SAV, 12.7 × 10^3 km^3 yr^{-1}). With values of ~7 × 10^3 km^3 yr^{-1}, croplands (CRO), and woody savannas (WSA) contribute equally to the total amount of global terrestrial ET, while the remaining 12 LCTs have much

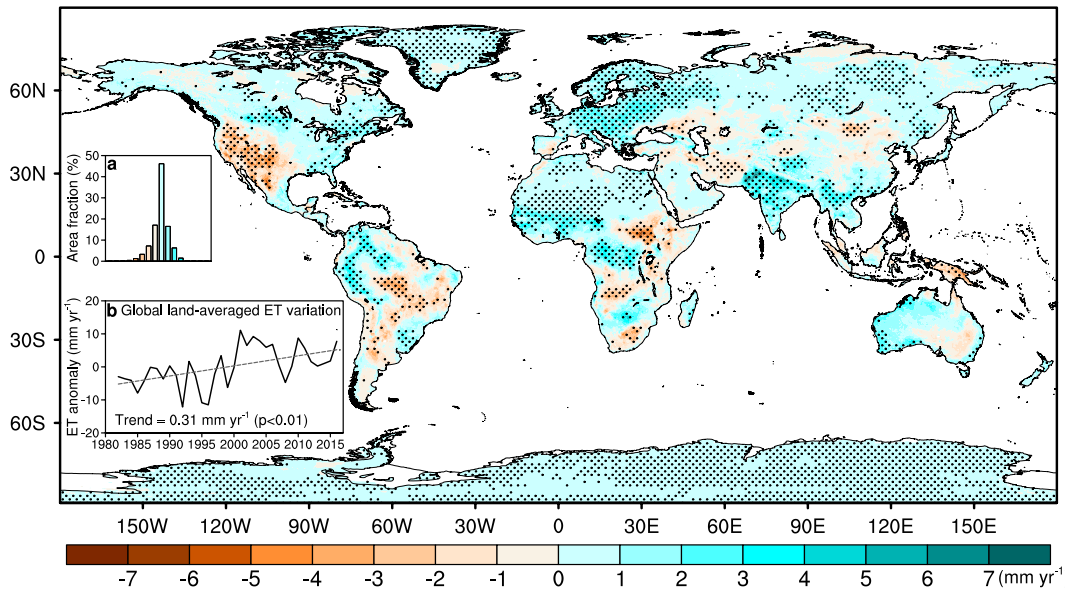

Figure 11. Spatial pattern of the trends (1982–2016) in annual evapotranspiration (ET) rates from the complementary relationship (CR) across the globe. The stippling indicates the trends that are statistically significant ($p < 0.05$). Inset (a) presents the land area fractions with different trends (and matching color) specified in the horizontal bar, while inset (b) displays the annual anomalies in global land-averaged ET rates during 1982–2016, with the dashed line denoting their least-squares-fitted linear trend.

smaller contributions, though cropland/natural vegetation mosaic (NVM) and deciduous broadleaf forests (DBF) produce annual ET rates in excess of 700 mm yr^{-1} (Table S4).

3.6. Long-Term Tendencies in Global ET Rates During 1982–2016

Figure 11 displays the spatial pattern of the estimated linear trends in annual ET rates from CR across the world during 1982–2016. As seen, annual ET rates have generally increased in the Northern Hemisphere. This is especially true for parts of the east-coast of North America, central/eastern Europe, western Sahel, northern India, the Tibetan Plateau, and most parts of Siberia where the strongest, statistically significant increases in ET occurred. However, significant decreases in ET occurred in the western United States, West Asia, and the Sudan region of Africa. In the Southern Hemisphere, significant increases in ET occurred mainly in Amazonia, the northern Andes, the Congo River basin, and western Australia while significant decreases in ET could be found in Papua New Guinea, certain regions in southern Africa, and the central and southern parts of South America. In general, the Southern Hemisphere has a proportionally larger area with decreasing ET rates than the Northern Hemisphere over the studied 35 years. It should be noted that the trends in ET shown in Figure 11 might be subject to obvious decadal variability and also the magnitude and sign of trends depend heavily on the exact period considered.

At the global scale, more than 70% (Figure 11, inset a) of the land area displays an increasing trend in annual ET rates during 1982–2016. Globally, terrestrial ET increased significantly with a tendency of 0.31 mm yr^{-1} ($p < 0.01$) over the last 35 years (Figure 11, inset b). The rate of increase in ET was stronger prior to 2000. During 2001–2008, annual ET significantly dropped at a rate of -1.8 mm yr^{-1} ($p < 0.01$), but it recovered fast since 2009.

The annual anomalies in the modeled ET rates of the CR and 11 of the ET products in Table 1 (note that MERRA2 was excluded from such a comparison because of its implausible inter-annual variability in ET, see Figure S7) plus the 20 CMIP6 models were further compared. Because eight ET products in Table 1 do not fully cover the global land (i.e., with no data in the deserts or Greenland/Antarctica), the comparison was made over vegetated surfaces only. As seen in Figure 12, inter-annual variations in the CR ET rates were overall within the range of the 11 main-stream ET products. For the global vegetated surface, the trend in annual ET during 1982–2016 from the CR (0.34 mm yr^{-1}, $p < 0.01$) is close to the median (0.28 mm yr^{-1}, $p < 0.01$) trend value of the main-stream

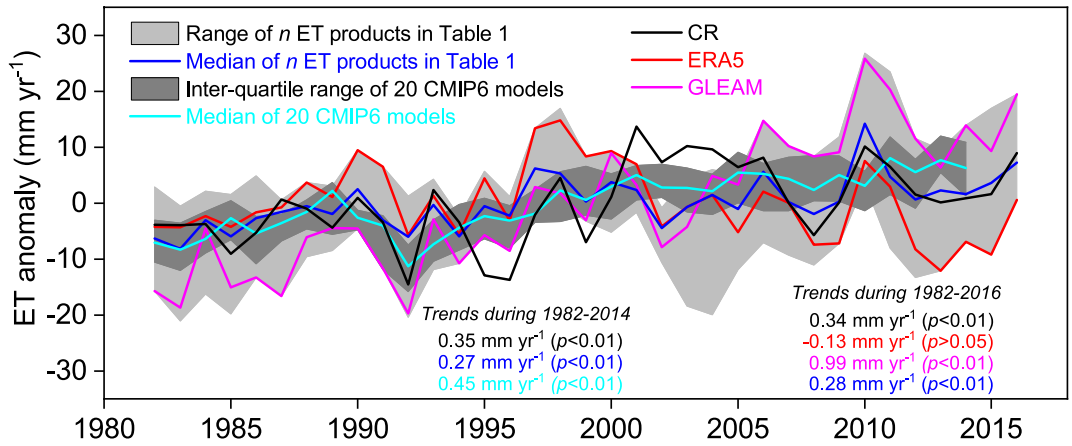

Figure 12. Annual anomalies in the global vegetated surface-averaged annual evapotranspiration (ET) rates from the complementary relationship (CR), ERA5, and Global Land Evaporation Amsterdam Model (GLEAM) during 1982–2016. The median value plus the range of the n ET products in Table 1 (excluding MERRA2) are also specified. Note the value of n here may vary by year according to the corresponding mutual overlap of the ET products, thus $n = 10$ (1982–2002), 11 (2003–2013), 9 (2014), and 5 (2015–2016), respectively. The inter-quartile range and the median of the 20 Coupled Model Inter-comparison Project Phase 6 (CMIP6) models during 1982–2014 are also displayed.

ET products in Table 1. Other two commonly used ET products with a global coverage, ERA5, and GLEAM, produce a very slight decreasing (−0.13 mm yr^{-1}, $p > 0.1$) and a much stronger significant increasing (0.99 mm yr^{-1}, $p < 0.01$) rate, respectively, in comparison with the median of these typical ET products (Figure 12).

The historical simulation from the CMIP6 models, though ends in 2014, also yields an increasing trend of 0.45 mm yr^{-1} ($p < 0.01$, Figure 12). For the same 1982–2014 period, the tendencies of the CR and the median of main-stream ET products in Table 1 are 0.35 and 0.27 mm yr^{-1} ($p < 0.01$ for both), respectively. The reason for the trend value discrepancy (i.e., 0.45 vs. 0.27 mm yr^{-1}) between the CMIP6 and the mainstream ET products is not clear yet. CMIP6 makes considerations to the rising atmospheric greenhouse gas concentrations, likely not included in most widely used current ET products (except PML_V2). However, rising CO_2 levels may also curtail rather than boost ET, via limiting stomata openings (Gedney et al., 2006; Xu et al., 2016), thus the loss of water from plants, thus making the larger ET trend value of CMIP6 somewhat uncertain. The CR with a trend value in between the median of CMIP6 and that of the main-stream ET products in Table 1, may correctly capture this possible ET reducing mechanism as it inherently accounts for the complex feedback mechanism that exists across the land-atmosphere interface.

4. Discussions

4.1. Advantages and Disadvantages of the CR Models in Large-Scale ET Estimation

As the CR employed in this study inherently builds upon the dynamic feedbacks between the land-atmosphere interface without the need of any soil and vegetation status or precipitation information while requiring only a minimal number of input variables (i.e., air temperature, air humidity, net radiation, and wind speed) in a calibration-free mode when applied on a global scale, it is probably the most versatile and simplest global ET estimation approach available today. From a spatial perspective, the value of its single, constant parameter, α, can be set independently of the model with the help of the forcing data only, as described in Szilagyi et al. (2017) and Ma and Szilagyi (2019), circumventing the necessity of any ground-truth ET data for calibration purposes. From a temporal perspective, the CR is able to yield historical ET series that other, more data intensive LSMs and RS models may not match in their temporal coverage. Note that net radiation in the CR can also be estimated from incoming global radiation or even from sunshine duration data only (Allen et al., 1998; Kim et al., 2019; Morton, 1983).

While the CR has previously been considered as a merely heuristic approach (McNaughton & Spriggs, 1989), a recent study by Szilagyi (2021) derived the current version from thermodynamic considerations and thus setting it on a stronger physical footing. The success of this version of the CR lies in its tracking the state of an air parcel,

in contact with the surface, via adiabatic processes. It directly relates the surface latent heat flux averaged over appropriate spatial and temporal scales to the average state of the air overlying the land surface and not through a proxy such as soil moisture or a vegetation index (Ma & Szilagyi, 2019). This CR version has already been demonstrated to outperform or match other available LSMs, RS models, atmospheric reanalysis and machine learning based-ET methods on a continental basis (e.g., Kim et al., 2019; Ma & Szilagyi, 2019; Ma et al., 2020, 2019).

It should be highlighted that the present CR-based ET model is substantially different from that of Brutsaert et al. (2020). The latter relies on global rainfall (not precipitation) data for a universal calibration of altogether seven model parameters, while the current CR model does not require such information, neither calibration. Also, the current CR version performs a dynamic scaling of the $E_w E_p^{-1}$ term in Equation 2 by a dynamic (i.e., updated in each time step) wetness index (i.e., $[E_p^{max} - E_p]\,[E_p^{max} - E_w]^{-1}$), while a similar scaling of $E_w E_p^{-1}$ in Brutsaert et al. (2020) is achieved through a temporally constant aridity index, containing the multiyear mean annual rainfall rate. This way, the current CR version was able to produce more reasonable trends in annual ET rates over the CONUS (Szilagyi et al., 2020) than that of Brutsaert et al. (2020).

Due to the temporal and spatial scale requirements for a fully developed dynamic equilibrium between the land and the overlying atmosphere, the present CR method is not recommended to be applied with an averaging period shorter than about five days (this latter to filter out the effect of any passing weather fronts (Morton, 1983)) and on a grid-resolution finer than about a kilometer-squared to allow for an adjustment of the atmospheric boundary layer to possible changes in land cover, land use or moisture status. For the same reason, the CR ET estimates need to be treated with caution near sudden jumps in surface wetness conditions, such as occur near land-sea boundaries, especially in hot and dry desert/semi-desert climates, where the corresponding potentially strong sea-breezes partially or fully disconnect the moisture status of the atmospheric boundary layer from the underlying land surface.

4.2. The Magnitudes of Global ET

The global multiyear (1982–2016) mean annual terrestrial ET rate from the CR is 500 ± 6 mm yr^{-1} (i.e., 72.3 ± 0.9 × 10^3 km^3 yr^{-1}). This value is within the range of the water-balance derived global land ET rate of 1.2–1.5 mm d^{-1} or 438–548 mm yr^{-1} by Wang and Dickinson (2012). When the desert and permanent ice/snow regions are excluded, the global vegetated-surface-averaged ET rate from the CR becomes 611 ± 7 mm yr^{-1} (i.e., 71.2 ± 0.7 × 10^3 km^3 yr^{-1}), a value close to the ensemble average of 606 ± 69 mm yr^{-1} from multiple diagnostic ET products by Mueller et al. (2011, Figure 1 therein) for the same spatial domain.

It should be noted that numerous studies exclude the desert and/or permanent ice and snow regions (e.g., Antarctica or Greenland) of the world where ET rates are usually very low. For this reason, a direct comparison of the global ET rate in the unit of millimeter without specifying the spatial domain of averaging may lead to significant confusions. Therefore, it is more reasonable to compare ET expressed in cubic kilometers because the deserts and permanent ice/snow regions of the world contribute little (less than 5%, according to Miralles et al., 2016) to the total amount of global terrestrial ET. With this in mind, the present CR-based ET amounts of 72.3 and 71.2 (× 10^3 km^3 yr^{-1}) are very close to previous results (Table S5) expressed in 10^3 km^3 yr^{-1}, for example, FLUXCOM (Jung et al., 2019): 76.0 (RS_METEO) and 75.6 (RS) both for 2001–2013; PLSH (K. Zhang et al., 2015): 74.3 (1982–2013); the Simple Terrestrial Evaporation to Atmosphere Model (STEAM, Wang-Erlandsson et al., 2014): 73.9 (2003–2017); GLEAM and the Priestley–Taylor Jet Propulsion Laboratory (PT-JPL; Miralles et al., 2016): 72.9 (note this is not the latest version 3.3a of GLEAM used in the present study) and 72.5, respectively, both for 2005–2007; PML_V2 (Y. Zhang et al., 2019): 72.8 (2003–2017); and the Water Balance model with Model Tree Ensemble (WB-MTE, Zeng et al., 2014): 71.1 (1982–2009). From an energy balance perspective, the global terrestrial latent heat flux was estimated to be 38.5 W m^{-1} (2000–2004) by Trenberth et al. (2009) and 38 W m^{-1} (2000–2005) by Wild et al. (2015), which translate to 71.4 and 70.5 (× 10^3 km^3 yr^{-1}), respectively. Note that, however, all above estimates are much higher than the results reported by (a) Oki and Kanae (2006): 65.5 × 10^3 km^3 yr^{-1} (period of averaging is not available), and; (b) Jung et al. (2010): 65 ± 3 × 10^3 km^3 yr^{-1} (1982–2008).

The multiyear mean global land precipitation (P) was estimated to be about (a) 117.6 × 10^3 km^3 yr^{-1} (1951–2000) by Schneider et al. (2017) from the GPCC data (involving an estimate for Antarctica), or; (b) 116.5 × 10^3 km^3 yr^{-1} (2000–2011) by Rodell et al. (2015) based on the Global Precipitation Climatology Project (GPCP) with

a global coverage. GRDC estimated the multiyear (1961–1990) mean annual terrestrial runoff (Q), without Antarctica, to be 41.9×10^3 km^3 yr^{-1} (Wilkinson et al., 2014). The global direct groundwater discharge to the oceans (Q_{gw}) by Zektser et al. (2006) was specified as $2.2–2.4 \times 10^3$ km^3 yr^{-1}. Although with differences in the averaging periods above for precipitation and discharge, the global multiyear mean water-balance ($P - Q - Q_{gw}$) ET amount is ~$72.2–73.5 \times 10^3$ km^3 yr^{-1}, which is on a par with the CR's estimated value of 72.3×10^3 km^3 yr^{-1} in the present study.

When taking the above-mentioned global land precipitation estimates from GPCC (Schneider et al., 2017) or from GPCP (Rodell et al., 2015) as reference, the CR yields a value of 62% for the global multiyear mean terrestrial ET ratio (i.e., ET/P). This result falls into the middle of the previously reported ET/P values: 58% by Alton et al. (2009) and Miralles et al. (2011); 59% by Oki and Kanae (2006); 62% by Müller Schmied et al. (2016); 63% by Wang-Erlandsson et al. (2014); 65% by Trenberth et al. (2007) and Mueller et al. (2013), and; 67% by Y. Zhang et al. (2016). It should be emphasized again that the present calibration-free CR method does not require any precipitation information (except for the sea-shore desert regions of Figure S1 where the land-atmosphere coupling significantly weakens), making it a fairly robust ET estimation choice for potential use in future global hydrological and climatological studies.

4.3. Temporal Variations in Global ET

The ongoing global warming due to increasing concentrations of greenhouse gases is expected to accelerate the hydrological cycle (Held & Soden, 2006; Huntington, 2006) because the atmospheric moisture holding capacity could increase by ~7% when air warms by 1°C based on the Clausius–Clapeyron relation (Schneider et al., 2010). One direct evidence for this speculation is that global near-surface specific humidity has increased with a rate of 0.07 g kg^{-1} decade^{-1} during 1973–2002 (Willett et al., 2007). Since changes in ET are energetically constrained, climate simulations suggested that the global evaporation (including the oceans) may increase with the air temperature at a rate of 2%–3% °C^{-1} (Schneider et al., 2010). However, decreasing pan evaporation rates in spite of the observed significant warming over the last few decades, initially reported by Peterson et al. (1995) and being referred to as the "evaporation paradox," were prevalent over most parts of the world (e.g., McVicar et al., 2012; Roderick & Farquhar, 2004; Y. Zhang et al., 2007). In this context, it was the CR that explained why the decrease in pan evaporation rates was in fact a signal of increasing land ET rates (Brutsaert & Parlange, 1998), though at that time (more than two decades ago) the variations in land ET remained lesser known owing to the dearth of global-scale ET products. The present CR ET estimates, in accordance with the available main-stream ET products and the coupled Earth System Models from CMIP6, suggest that the global terrestrial ET rate did increase from the early 1980s to the late 1990s (Figure 12).

However, the CR modeled global land ET rates started to decrease with 2001, which was especially apparent until 2008 (see the inset in Figure 11). In fact, the contrasting trends before and after the year 2000 are not only true for the CR but also for other available ET products, as illustrated by the multi-model synthesis of Mueller et al. (2013, Figure 3 therein). Jung et al. (2010) attributed the significant reduction in global terrestrial ET during 1998–2008 to generally declining soil moisture conditions in the Southern Hemisphere. Although Figure 11 is for 1982–2016, it is apparent that the Southern Hemisphere did have a higher percentage of regions with decreasing ET rates than the Northern Hemisphere, similar to the results reported by Jung et al. (2010, Figure 3a therein) for a relatively shorter period.

Miralles et al. (2014) further demonstrated that the multi-decadal variability of terrestrial ET is largely controlled by the dynamics of El Niño/Southern Oscillation (ENSO). They explained that the decline of ET in the first decade of the 21st century was mainly because El Niño led to reduced precipitation rates over Amazonia, Africa, Australia, and Indonesia, thereby resulting in lower soil water content and thus cutting back on ET. Interestingly, however, La Niña became dominant since 2009 (see Figure 1c in Miralles et al., 2014), bringing enhanced terrestrial precipitation rates, thus bolstering ET again. These ENSO events perfectly explain the CR modeled annual ET rates post-2000 (Figure 11 inset b). A more recent study by Kim et al. (2019, Figure 5 therein) also found that the current CR model was able to capture the influences of ENSO on ET over the CONUS.

In addition to climatic controls on ET, the wide-spread greening of Earth over the past few decades (Piao et al., 2019; Zhu et al., 2016) may bolster global terrestrial ET rates since increased LAI could enhance not only

transpiration but also the evaporation of the canopy interception, as has been reported by multiple studies (e.g., Piao et al., 2019; Zeng, Peng, & Piao, 2018; K. Zhang et al., 2015; Y. Zhang et al., 2016). At the global scale, it has been found that a unit increase in LAI enlarged the latent heat flux by 3.66 ± 0.45 W m^{-2} during 1982–2016, but such an impact of the vegetation on ET appears less apparent in humid regions than in arid ones (Forzieri et al., 2020). Coupled climate modeling by Zeng, Piao, et al. (2018) proposed that the increase in LAI during 1982–2011 may have led to an increase of 12 ± 2.4 mm yr^{-1} in global land ET rates. Interestingly, the present CR-simulated ET rates over the global vegetated surface also display an increasing trend through the modeled 35 years (Figure 12), yielding an overall identical increase of 11.9 mm, even though it did not use any vegetation data as input. While the CR method does not explicitly account for the effects of vegetation change on ET, it indirectly takes it into consideration via the variations in temperature, humidity, wind speed, and net radiation, which are all impacted by changes in land surface properties.

4.4. Potential Uncertainties in the Validations

While the water-balance-estimated annual ET_{wb} rates from a great number of basins with varying climates and land covers have been used here to assess not only the CR but also another 12 main-stream ET products, such evaluations mainly concentrate on data rich areas where all of these models are constrained by generally high quality ground observations. For data scarce regions in the world, however, the accuracy of any ET products including the CR remains less studied. A similar concern holds also for the validations of the CR estimates by the FLUXNET data, as most EC towers are located in North America, Europe, and Australia, while much fewer are situated in Asia, Africa, and South America (see Figure 1a). Besides, most FLUXNET towers are for grasslands and forests that are located in mild climatic regions, while the number of EC towers for other LCTs and for extreme humid and arid regions is much lower (see Table S1). For example, only eight EBF sites were used to assess the CR's performance. While the median NSE value for this LCT is negative in Figure 2a, the validations using ET_{wb} in the Amazon and Congo Basins, where most EBF are found, do not show significant bias (see Figure 4a for Basins #47, #48, #49, and #17). Therefore, the model validation results against FLUXNET EC measurements should be interpreted with some caution.

It should be emphasized that even for basins where measured runoff data are available, the accuracy of ET_{wb}, as we described previously, depends strongly on the quality of precipitation data since the meteorological stations may have a poor spatial coverage in many parts of the world, for example, in high latitudes (see Figure 2 in Schneider et al., 2017), which may lead to a misrepresentation of basin-wide ET_{wb}. This way the confidence of model evaluations against the water balance approach in this study may degrade to some extent for basins in boreal regions.

4.5. Lessons Learned From the Present Multi-Model Evaluations

We note that poor validation results of any ET products (e.g., VIC_GL and MERRA2) by ET_{wb} values do not necessarily mean that a given ET model is inferior to others. Instead, the reliability of the meteorological forcing and/or the parameter values determined by gridded vegetation and/or soil data also impact a model's ability to estimate ET. The sensitivity study by Badgley et al. (2015) suggested that the span of global annual ET rates in a typical year could reach 100 mm yr^{-1} when different forcing were used to drive the PT-JPL model of Fisher et al. (2008). Such a finding can also be partially evidenced by the diverse performances of the three FLUXCOM ET products displayed in Figures 5d–5f and S2d–S2f, which were driven by three different meteorological forcing (Jung et al., 2019).

Regarding the current calibration-free CR model, the sensitivity of the modeled ET rates to meteorological forcing has been illustrated by Ma et al. (2019). While a wide range of evaluations suggested that the ERA5 forcing is indeed more accurate than other atmospheric reanalyzes with regard to radiation (e.g., He et al., 2021), air temperature (e.g., Martens et al., 2020; Tarek et al., 2020), wind speed and humidity (e.g., Graham et al., 2019), the potential error in this particular forcing is certainly not negligible, which may affect the accuracy of this new CR-based ET product. To illustrate the impact of different meteorological forcing on the current CR model, the modeled ET (driven mainly by ERA5) of this study are compared to previous ET estimates of the same CR model but driven by T_a and T_d from PRISM as well as R_n and U_{10} from NARR (Ma & Szilagyi, 2019) for 18 basins cover-

ing the CONUS (i.e., Basin #29–46 in Figure 1b). Note that PRISM and NARR were specifically designed for the CONUS, therefore may be more reliable there than ERA5 assembled for a global coverage. As seen in Figure S8, the R between the two modeled ET rates reaches 0.987 and the RMSE is less than 50 mm yr^{-1}. Moreover, the inter-annual variability of the basin-averaged ET rates is almost identical (i.e., vertical and horizontal whiskers are close in length) between the two ET estimates driven by different meteorological forcing. This suggests that the ERA5 forcing may indeed be appropriate for the simulation of global terrestrial ET rates. Even so, we argue that a continued refinement of model forcing is a key step in reducing uncertainties in any future ET models, including the CR; though this is beyond the scope of the present study.

A final caveat for large-scale ET modeling, including the CR, is that the resulting ET rates should be further tested/verified by embedding them into different hydrological models (either physically based or conceptual spatially lumped/distributed parameter ones) to see whether they improve such modeling efforts by mitigating the non-closure of the water balance characteristic of these models, as has been documented by a wide range of studies (e.g., Sahoo et al., 2011; Sheffield et al., 2009). As the present CR model is calibration-free and avoids the uncertainties found in soil, vegetation, and precipitation inputs, it may offer a potential way forward to improve the water budget closure at basin-to-global scales when coupled to hydrological models, thus, deserving further study in the future.

5. Conclusions

Having recognized the challenges in (a) explicitly resolving global-scale soil and vegetation data, and; (b) precipitation forcing, this study estimates global terrestrial ET rates over a 35-year period with a recently developed calibration-free CR model, which not only avoids the uncertainties mentioned above but also dispenses with the need of "prior" measured ET data for model calibration. While this CR model was forced by global reanalysis data and employed a temporally and spatially constant PT α value derived from the forcing data, the modeled ET rates show a good agreement with (a) locally measured EC data, as more than 70% of the 129 global FLUXNET sites display NSE values in excess of 0.5, and; (b) water balance-based ET_{wb} of 52 river basins, encompassing diverse climates and land covers across the world producing an NSE value of 0.93 for multiyear averages and 0.88 for annual values, and thus indicating that the model is able to accurately simulate land ET rates globally. Further evaluations of another 12 main-stream global ET products reveal that this new CR-based ET approach is on a par with the currently available ET products, as evidenced by typically improved statistical metrics at varying time scales. All in all, the present CR model is well-suited for facilitating terrestrial ET studies on a global scale.

The multiyear mean global land ET rate specified by the CR is 500 ± 6 mm yr^{-1} ($72.3 \pm 0.9 \times 10^3$ km^3 yr^{-1}). During 1982–2016, more than 70% of the global land area exhibited increasing trends in the modeled ET, while significant decreases in ET rates occurred mainly in the western United States, central, and southern South America, in certain regions of Africa (especially the Sudan), Asia, and the majority of Papua New Guinea. Globally, the land-averaged ET increased significantly with a rate of 0.31 mm yr^{-1} over the 35 years modeled. This means that global land ET increased by 2.2% during 1982–2016. The increase in CR ET is more obvious prior to the year 2000, and was replaced by a decreasing one after that, which was then followed by global ET rates recovery since 2009. Model inter-comparisons suggest that, both climatology and trends in global ET rates produced by the CR, stay close to the median of not only the current main-stream ET products but also to those of 20 CMIP6 models for a slightly different period. Although the present study only covers the 1982–2016 period because of the availability of inputs, regular annual updates of this global CR ET product are planned.

As the current CR model is calibration-free (when applied over a large enough region to encompass periodically or permanently wet land surfaces) and requires no precipitation (except in sea-shore deserts for an ET-value correction), vegetation, or soil characteristics information, while employs a very limited number of meteorological variables as input to a single, non-dimensional equation, it has the potential for users to estimate ET rates not only on a global scale but also over any large regions (with probably improved local forcing) and/or periods chosen (even as long as a century since the model's net radiation input may also be derived from more commonly recorded sunshine duration data). In addition, considering its highly parsimonious model structure, this CR model could easily be incorporated into more complex hydrological and/or climate models, leading to potentially improved large-scale hydrological and climate simulations.

Data Availability Statement

All data used in this study can be accessed from the websites as following: FLUXNET2015 (https://fluxnet.org/data/fluxnet2015-dataset/); GPCC precipitation (https://opendata.dwd.de/climate_environment/GPCC/html/fulldata-monthly_v2018_doi_download.html); PRISM precipitation (http://prism.oregonstate.edu/); GRDC runoff (https://www.bafg.de/GRDC/EN/Home/homepage_node.html); USGS runoff (https://waterwatch.usgs.gov/?id=wwds_runoff); China Sediment Bulletin runoff (http://www.mwr.gov.cn/sj/tjgb/zghlnsgb/); GRACE (https://grace.jpl.nasa.gov/data/get-data/jpl_global_mascons/); GRACE-REC (https://doi.org/10.6084/m9.figshare.7670849); ERA5 and ERA5-Land data (https://www.ecmwf.int/en/forecasts/datasets/reanalysis-datasets/era5); CERES Rn (https://ceres.larc.nasa.gov/); GLASS albedo and emissivity (http://www.glass.umd.edu/Download.html); MODIS land cover type (https://lpdaac.usgs.gov/products/mcd12c1v006/); MERRA2 (https://disc.gsfc.nasa.gov/datasets/M2TMNXLND_5.12.4/summary?keywords=MERRA-2); JRA55 (https://jra.kishou.go.jp/JRA-55/index_en.html#jra-55); FLUXCOM (https://www.bgc-jena.mpg.de/geodb/projects/Home.php); Noah_GL (https://disc.gsfc.nasa.gov/datasets/GLDAS_NOAH025_M_2.0/summary?keywords=GLDAS); CLSM_GL (https://disc.gsfc.nasa.gov/datasets/GLDAS_CLSM10_M_2.0/summary?keywords=GLDAS); VIC_GL (https://disc.gsfc.nasa.gov/datasets/GLDAS_VIC10_M_2.0/summary?keywords=GLDAS); GLEAM (https://www.gleam.eu/); PLSH (http://files.ntsg.umt.edu/data/ET_global_monthly/Global_8kmResolution/); PML_V2 (https://code.earthengine.google.com/?asset=projects/pml_evapotranspiration/PML/OUTPUT/PML_V2_8day_v014); and CMIP6 historical simulations (https://esgf-node.llnl.gov/search/cmip6/). The newly developed ET product using the CR method is available at https://doi.org/10.6084/m9.figshare.13634552.

Acknowledgments
This research was jointly funded by the Second Tibetan Plateau Scientific Expedition and Research Program (2019QZKK0208), National Natural Science Foundation of China (41801047 and 41971032), CAS Pioneer Talents Program, CAS-CSIRO International Cooperation Program, the TKP2020 BME-IKA-VÍZ program, and the Open Research Fund Program of State Key Laboratory of Cryospheric Science, Northwest Institute of Eco-Environment and Resources, CAS (SKLCS-OP-2020-11). We thank all related organizations and persons for making the data listed in the Data Availability Statement available to the public. In particular, we are grateful to GRDC and FLUXNET for sharing the measured runoff and ET data, respectively. Special thanks to the Associate Editor and three anonymous reviewers for their valuable comments.

References

Allen, R. G, Pereira, L. S, Raes, D, & Smith, M (1998). *Crop evapotranspiration: Guidelines for computing crop water requirements. In: FAO Irrigation and drainage paper 56*. Food and Agriculture Organization of the United Nations, (p. 300).

Alton, P., Fisher, R., Los, S., & Williams, M. (2009). Simulations of global evapotranspiration using semiempirical and mechanistic schemes of plant hydrology. *Global Biogeochemical Cycles*, *23*(4). https://doi.org/10.1029/2009gb003540

Badgley, G., Fisher, J. B., Jiménez, C., Tu, K. P., & Vinukollu, R. (2015). On uncertainty in global terrestrial evapotranspiration estimates from choice of input forcing datasets. *Journal of Hydrometeorology*, *16*, 1449–1455. https://doi.org/10.1175/JHM-D-14-0040.1

Baldocchi, D. D. (2020). How eddy covariance flux measurements have contributed to our understanding of Global Change Biology. *Global Change Biology*, *26*(1), 242–260. https://doi.org/10.1111/gcb.14807

Baldocchi, D. D., Falge, E., Gu, L., Olson, R., Hollinger, D., Running, S., et al. (2001). FLUXNET: A new tool to study the temporal and spatial variability of ecosystem-scale carbon dioxide, water vapor, and energy flux densities. *Bulletin of the American Meteorological Society*, *82*(11), 2415–2434. https://doi.org/10.1175/1520-0477(2001)082<2415:fantts>2.3.co;2

Beaudoing, H., & Rodell, M. (2019). *GLDAS Noah land surface model L4 monthly 0.25 × 0.25 degree V2.0. Greenbelt*. Goddard Earth Sciences Data and Information Services Center (GES DISC). https://doi.org/10.5067/9SQ1B3ZXP2C5

Beaudoing, H., & Rodell, M. (2020). *GLDAS VIC land surface model L4 monthly 1.0 × 1.0 degree V2.0. Greenbelt*. Goddard Earth Sciences Data and Information Services Center (GES DISC). https://doi.org/10.5067/ZRIHVF29X43C

Becker, A., Finger, P., Meyer-Christoffer, A., Rudolf, B., Schamm, K., Schneider, U., & Ziese, M. (2013). A description of the global land-surface precipitation data products of the global precipitation climatology centre with sample applications including centennial (trend) analysis from 1901-present. *Earth System Science Data*, *5*, 71–99. https://doi.org/10.5194/essd-5-71-2013

Bouchet, R. J. (1963). Evapotranspiration réelle et potentielle, signification climatique. *International Association of Scientific Hydrology, Publication*, *62*, 134–136. https://doi.org/10.1080/02626666309493366

Brutsaert, W. (2005). *Hydrology: An introduction*. Cambridge University Press.

Brutsaert, W. (2015). A generalized complementary principle with physical constraints for land-surface evaporation. *Water Resources Research*, *51*(10), 8087–8093. https://doi.org/10.1002/2015WR017720

Brutsaert, W., Cheng, L., & Zhang, L. (2020). Spatial distribution of global landscape evaporation in the early twenty first century by means of a generalized complementary approach. *Journal of Hydrometeorology*, *21*(2), 287–298. https://doi.org/10.1175/jhm-d-19-0208.1

Brutsaert, W., & Parlange, M. B. (1998). Hydrologic cycle explains the evaporation paradox. *Nature*, *396*, 30. https://doi.org/10.1038/23845

Brutsaert, W., & Stricker, H. (1979). An advection-aridity approach to estimate actual regional evapotranspiration. *Water Resources Research*, *15*(2), 443–450. https://doi.org/10.1029/wr015i002p00443

Budyko, M. I. (1974). *Climate and life*. Academic Press.

Chen, J. M., & Liu, J. (2020). Evolution of evapotranspiration models using thermal and shortwave remote sensing data. *Remote Sensing of Environment*, *237*, 111594. https://doi.org/10.1016/j.rse.2019.111594

Clark, M. P., & Slater, A. G. (2006). Probabilistic quantitative precipitation estimation in complex terrain. *Journal of Hydrometeorology*, *7*(1), 3–22. https://doi.org/10.1175/JHM474.1

Crago, R., & Qualls, R. (2018). Evaluation of the generalized and rescaled complementary evaporation relationships. *Water Resouces Research*, *54*(10), 8086–8102. https://doi.org/10.1029/2018WR023401

Cuntz, M., Mai, J., Samaniego, L., Clark, M., Wulfmeyer, V., Branch, O., et al. (2016). The impact of standard and hard-coded parameters on the hydrologic fluxes in the Noah-MP land surface model. *Journal of Geophysical Research: Atmospheres*, *121*(18), 10676–10700. https://doi.org/10.1002/2016jd025097

Dai, Y., Shangguan, W., Wei, N., Xin, Q., Yuan, H., Zhang, S., et al. (2019). A review of the global soil property maps for Earth system models. *Soil*, *5*(2), 137–158. https://doi.org/10.5194/soil-5-137-2019

Daly, C., Halbleib, M., Smith, J. I., Gibson, W. P., Doggett, M. K., Taylor, G. H., et al. (2008). Physiographically sensitive mapping of climatological temperature and precipitation across the conterminous United States. *International Journal of Climatology*, *28*(15), 2031–2064. https://doi.org/10.1002/joc.1688

Dennis, E. J., & Berbery, E. H. (2021). The role of soil texture in local land surface–atmosphere coupling and regional climate. *Journal of Hydrometeorology*, *22*(2), 313–330. https://doi.org/10.1175/jhm-d-20-0047.1

Eyring, V., Bony, S., Meehl, G. A., Senior, C. A., Stevens, B., Stouffer, R. J., & Taylor, K. E. (2016). Overview of the coupled model intercomparison project phase 6 (CMIP6) experimental design and organization. *Geoscientific Model Development*, *9*(5), 1937–1958. https://doi.org/10.5194/gmd-9-1937-2016

Fang, H., Baret, F., Plummer, S., & Schaepman-Strub, G. (2019). An overview of global leaf area index (LAI): Methods, products, validation, and applications. *Reviews of Geophysics*, *57*(3), 739–799. https://doi.org/10.1029/2018rg000608

Fisher, J. B., Melton, F., Middleton, E., Hain, C., Anderson, M., Allen, R., et al. (2017). The future of evapotranspiration: Global requirements for ecosystem functioning, carbon and climate feedbacks, agricultural management, and water resources. *Water Resources Research*, *53*(4), 2618–2626. https://doi.org/10.1002/2016wr020175

Fisher, J. B., Tu, K. P., & Baldocchi, D. D. (2008). Global estimates of the land–atmosphere water flux based on monthly AVHRR and ISLSCP-II data, validated at 16 FLUXNET sites. *Remote Sensing of Environment*, *112*(3), 901–919. https://doi.org/10.1016/j.rse.2007.06.025

Forzieri, G., Miralles, D. G., Ciais, P., Alkama, R., Ryu, Y., Duveiller, G., et al. (2020). Increased control of vegetation on global terrestrial energy fluxes. *Nature Climate Change*, *10*, 356–362. https://doi.org/10.1038/s41558-020-0717-0

Gao, B., & Xu, X. (2020). Derivation of an exponential complementary function with physical constraints for land surface evaporation estimation. *Journal of Hydrology*, *593*, 125623. https://doi.org/10.1016/j.jhydrol.2020.125623

Gedney, N., Cox, P. M., Betts, R. A., Boucher, O., Huntingford, C., & Stott, P. A. (2006). Detection of a direct carbon dioxide effect in continental river runoff records. *Nature*, *439*, 835–838. https://doi.org/10.1038/nature04504

Gelaro, R., McCarty, W., Suarez, M. J., Todling, R., Molod, A., Takacs, L., et al. (2017). The modern-era retrospective analysis for research and applications, version 2 (MERRA-2). *Journal of Climate*, *30*(13), 5419–5454. https://doi.org/10.1175/JCLI-D-16-0758.1

Graham, R. M., Hudson, S. R., & Maturilli, M. (2019). Improved performance of ERA5 in Arctic Gateway relative to four global atmospheric reanalyses. *Geophysical Research Letters*, *46*(11), 6138–6147. https://doi.org/10.1029/2019gl082781

Han, J., Yang, Y., Roderick, M. L., McVicar, T. R., Yang, D., Zhang, S., & Beck, H. E. (2020). Assessing the steady-state assumption in water balance calculation across global catchments. *Water Resources Research*, *56*(7), e2020WR027392. https://doi.org/10.1029/2020wr027392

Han, S., & Tian, F. (2018). Derivation of a sigmoid generalized complementary function for evaporation with physical constraints. *Water Resources Research*, *54*(7), 5050–5068. https://doi.org/10.1029/2017WR021755

Han, S., & Tian, F. (2020). A review of the complementary principle of evaporation: From the original linear relationship to generalized nonlinear functions. *Hydrology and Earth System Sciences*, *24*, 2269–2285. https://doi.org/10.5194/hess-24-2269-2020

Harris, I., Osborn, T. J., Jones, P., & Lister, D. (2020). Version 4 of the CRU TS monthly high-resolution gridded multivariate climate dataset. *Scientific Data*, *7*(1), 1–18. https://doi.org/10.1038/s41597-020-0453-3

Held, I. M., & Soden, B. J. (2006). Robust responses of the hydrological cycle to global warming. *Journal of Climate*, *19*(21), 5686–5699. https://doi.org/10.1175/JCLI3990.1

Hersbach, H., Bell, B., Berrisford, P., Hirahara, S., Horányi, A., Muñoz-Sabater, J., et al. (2020). The ERA5 global reanalysis. *Quarterly Journal of the Royal Meteorological Society*, *146*, 1999–2049. https://doi.org/10.1002/qj.3803

He, Y., Wang, K., & Feng, F. (2021). Improvement of ERA5 over ERA-interim in simulating surface incident solar radiation throughout China. *Journal of Climate*, *34*(10), 3853–3867. https://doi.org/10.1175/JCLI-D-20-0300.1

Humphrey, V., & Gudmundsson, L. (2019). GRACE-REC: A reconstruction of climate-driven water storage changes over the last century. *Earth System Science Data*, *11*, 1153–1170. https://doi.org/10.5194/essd-11-1153-2019

Humphrey, V., Zscheischler, J., Ciais, P., Gudmundsson, L., Sitch, S., & Seneviratne, S. I. (2018). Sensitivity of atmospheric CO2 growth rate to observed changes in terrestrial water storage. *Nature*, *560*(7720), 628–631. https://doi.org/10.1038/s41586-018-0424-4

Huntington, T. G. (2006). Evidence for intensification of the global water cycle: Review and synthesis. *Journal of Hydrology*, *319*(1–4), 83–95. https://doi.org/10.1016/j.jhydrol.2005.07.003

Jiang, C., Ryu, Y., Fang, H., Myneni, R., Claverie, M., & Zhu, Z. (2017). Inconsistencies of interannual variability and trends in long-term satellite leaf area index products. *Global Change Biology*, *23*(10), 4133–4146. https://doi.org/10.1111/gcb.13787

Jung, M., Koirala, S., Weber, U., Ichii, K., Gans, F., Camps-Valls, G., et al. (2019). The FLUXCOM ensemble of global land-atmosphere energy fluxes. *Scientific Data*, *6*, 1–14. https://doi.org/10.1038/s41597-019-0076-8

Jung, M., Reichstein, M., Ciais, P., Seneviratne, S. I., Sheffield, J., Goulden, M. L., et al. (2010). Recent decline in the global land evapotranspiration trend due to limited moisture supply. *Nature*, *467*(7318), 951–954. https://doi.org/10.1038/nature09396

Kato, S., Rose, F. G., Rutan, D. A., Thorsen, T. J., Loeb, N. G., Doelling, D. R., et al. (2018). Surface irradiances of edition 4.0 clouds and the Earth's radiant energy system (CERES) energy balanced and filled (EBAF) data product. *Journal of Climate*, *31*(11), 4501–4527. https://doi.org/10.1175/jcli-d-17-0523.1

Kim, D., Lee, W.-S., Kim, S. T., & Chun, J. A. (2019). Historical drought assessment over the contiguous United States using the generalized complementary principle of evapotranspiration. *Water Resources Research*, *55*(7), 6244–6267. https://doi.org/10.1029/2019WR024991

Kim, H. (2017). *Global soil wetness project Phase 3 atmospheric boundary conditions (experiment 1). Data integration and Analysis system (DIAS) (Dataset)*. https://doi.org/10.20783/DIAS.501

Kim, S., Anabalón, A., & Sharma, A. (2021). An assessment of concurrency in evapotranspiration trends across multiple global datasets. *Journal of Hydrometeorology*, *22*(1), 231–244. https://doi.org/10.1175/JHM-D-20-0059.1

Kobayashi, S., Ota, Y., Harada, Y., Ebita, A., Moriya, M., Onoda, H., et al. (2015). The JRA-55 reanalysis: General specifications and basic characteristics. *Journal of the Meteorological Society of Japan*, *93*(1), 5–48. https://doi.org/10.2151/jmsj.2015-001

Kyatengerwa, C., Kim, D., & Choi, M. (2020). A national-scale drought assessment in Uganda based on evapotranspiration deficits from the Bouchet hypothesis. *Journal of Hydrology*, *580*, 124348. https://doi.org/10.1016/j.jhydrol.2019.124348

Lawrence, D. M., Fisher, R. A., Koven, C. D., Oleson, K. W., Swenson, S. C., Bonan, G., et al. (2019). The Community Land Model Version 5: Description of new features, benchmarking, and impact of forcing uncertainty. *Journal of Advances in Modeling Earth Systems*, *11*(12), 4245–4287. https://doi.org/10.1029/2018ms001583

Liang, S., Cheng, J., Jia, K., Jiang, B., Liu, Q., Xiao, Z., et al. (2021). The Global LAnd Surface Satellite (GLASS) product suite. *Bulletin of the American Meteorological Society*, *102*(2), E323–E337. https://doi.org/10.1175/bams-d-18-0341.1

Li, B., Rodell, M., Sheffield, J., Wood, E., & Sutanudjaja, E. (2019). Long-term, non-anthropogenic groundwater storage changes simulated by three global-scale hydrological models. *Scientific Reports*, *9*(1), 10746. https://doi.org/10.1038/s41598-019-47219-z

Li, X., Cheng, G., Liu, S., Xiao, Q., Ma, M., Jin, R., et al. (2013). Heihe watershed allied telemetry experimental research (HiWATER): Scientific objectives and experimental design. *Bulletin of the American Meteorological Society*, *94*(8), 1145–1160. https://doi.org/10.1175/bams-d-12-00154.1

Lundquist, J., Hughes, M., Gutmann, E., & Kapnick, S. (2019). Our skill in modeling mountain rain and snow is bypassing the skill of our observational networks. *Bulletin of the American Meteorological Society*, *100*(12), 2473–2490. https://doi.org/10.1175/bams-d-19-0001.1

Lundquist, J., Hughes, M., Henn, B., Gutmann, E. D., Livneh, B., Dozier, J., & Neiman, P. (2015). High-elevation precipitation patterns: Using snow measurements to assess daily gridded datasets across the Sierra Nevada, California. *Journal of Hydrometeorology*, *16*(4), 1773–1792. https://doi.org/10.1175/jhm-d-15-0019.1

Lyapustin, A., Wang, Y., Xiong, X., Meister, G., Platnick, S., Levy, R., et al. (2014). Scientific impact of MODIS C5 calibration degradation and C6+ improvements. *Atmospheric Measurement Techniques*, *7*(12), 4353–4365. https://doi.org/10.5194/amt-7-4353-2014

Müller Schmied, H., Adam, L., Eisner, S., Fink, G., Flörke, M., Kim, H., et al. (2016). Variations of global and continental water balance components as impacted by climate forcing uncertainty and human water use. *Hydrology and Earth System Sciences*, *20*(7), 2877–2898. https://doi.org/10.5194/hess-20-2877-2016

Ma, N., Niu, G.-Y., Xia, Y., Cai, X., Zhang, Y., Ma, Y., & Fang, Y. (2017). A systematic evaluation of Noah-MP in simulating landatmosphere energy, water, and carbon exchanges over the continental United States. *Journal of Geophysical Research: Atmospheres*, *122*, 12245–12268. https://doi.org/10.1002/2017JD027597

Ma, N., & Szilagyi, J. (2019). The CR of evaporation: A calibration-free diagnostic and benchmarking tool for large-scale terrestrial evapotranspiration modeling. *Water Resources Research*, *55*(8), 7246–7274. https://doi.org/10.1029/2019wr024867

Ma, N., Szilagyi, J., & Jozsa, J. (2020). Benchmarking large-scale evapotranspiration estimates: A perspective from a calibration-free complementary relationship approach and FLUXCOM. *Journal of Hydrology*, *590*, 125221. https://doi.org/10.1016/j.jhydrol.2020.125221

Ma, N., Szilagyi, J., Zhang, Y., & Liu, W. (2019). Complementary-relationship-based modeling of terrestrial evapotranspiration across China during 1982–2012: Validations and spatiotemporal analyses. *Journal of Geophysical Research: Atmospheres*, *124*(8), 4326–4351. https://doi.org/10.1029/2018jd029850

Ma, N., Zhang, Y., Szilagyi, J., Guo, Y., Zhai, J., & Gao, H. (2015a). Evaluating the complementary relationship of evapotranspiration in the alpine steppe of the Tibetan Plateau. *Water Resources Research*, *51*(2), 1069–1083. https://doi.org/10.1002/2014wr015493

Ma, N., Zhang, Y., Xu, C.-Y., & Szilagyi, J. (2015b). Modeling actual evapotranspiration with routine meteorological variables in the datascarce region of the Tibetan Plateau: Comparisons and implications. *Journal of Geophysical Research: Biogeosciences*, *120*, 1638–1657. https://doi.org/10.1002/2015JG003006

Martens, B., Miralles, D. G., Lievens, H., van der Schalie, R., de Jeu, R. A. M., Fernández-Prieto, D., et al. (2017). GLEAM v3: Satellite-based land evaporation and root-zone soil moisture. *Geoscientific Model Development*, *10*(5), 1903–1925. https://doi.org/10.5194/gmd-10-1903-2017

Martens, B., Schumacher, D. L., Wouters, H., Muñoz-Sabater, J., Verhoest, N. E. C., & Miralles, D. G. (2020). Evaluating the land-surface energy partitioning in ERA5. *Geoscientific Model Development*, *13*(9), 4159–4181. https://doi.org/10.5194/gmd-13-4159-2020

McNaughton, K. G., & Spriggs, T. W. (1989). *An evaluation of the Priestley and Taylor equation and the complementary relationship using results from a mixed-layer model of the convective boundary layer. In: Estimation of Areal Evapoiranspiration*.

McVicar, T. R., Roderick, M. L., Donohue, R. J., Li, L. T., Van Niel, T. G., Thomas, A., et al. (2012). Global review and synthesis of trends in observed terrestrial near-surface wind speeds: Implications for evaporation. *Journal of Hydrology*, *416–417*, 182–205. https://doi.org/10.1016/j.jhydrol.2011.10.024

Miralles, D. G., De Jeu, R. A. M., Gash, J. H., Holmes, T. R. H., & Dolman, A. J. (2011). Magnitude and variability of land evaporation and its components at the global scale. *Hydrology and Earth System Sciences*, *15*(3), 967–981. https://doi.org/10.5194/hess-15-967-2011

Miralles, D. G., Jiménez, C., Jung, M., Michel, D., Ershadi, A., McCabe, M. F., et al. (2016). The WACMOS-ET project-Part 2: Evaluation of global terrestrial evaporation data sets. *Hydrology and Earth System Sciences*, *20*(2), 823–842. https://doi.org/10.5194/hess-20-823-2016

Miralles, D. G., van den Berg, M. J., Gash, J. H., Parinussa, R. M., de Jeu, R. A. M., Beck, H. E., et al. (2014). El Niño-La Niña cycle and recent trends in continental evaporation. *Nature Climate Change*, *4*, 122–126. https://doi.org/10.1038/nclimate2068

Morton, F. I. (1983). Operational estimates of areal evapotranspiration and their significance to the science and practice of hydrology. *Journal of Hydrology*, *66*(1–4), 1–76. https://doi.org/10.1016/0022-1694(83)90177-4

Mueller, B., Hirschi, M., Jimenez, C., Ciais, P., Dirmeyer, P. A., Dolman, A. J., et al. (2013). Benchmark products for land evapotranspiration: LandFlux-EVAL multi-data set synthesis. *Hydrology and Earth System Sciences*, *17*(10), 3707–3720. https://doi.org/10.5194/hess-17-3707-2013

Mueller, B., Seneviratne, S. I., Jimenez, C., Corti, T., Hirschi, M., Balsamo, G., et al. (2011). Evaluation of global observations-based evapotranspiration datasets and IPCC AR4 simulations. *Geophysical Research Letters*, *38*(6). https://doi.org/10.1029/2010gl046230

Novick, K. A., Biederman, J. A., Desai, A. R., Litvak, M. E., Moore, D. J. P., Scott, R. L., & Torn, M. S. (2018). The AmeriFlux network: A coalition of the willing. *Agricultural and Forest Meteorology*, *249*, 444–456. https://doi.org/10.1016/j.agrformet.2017.10.009

Oki, T., & Kanae, S. (2006). Global hydrological cycles and world water resources. *Science*, *313*(5790), 1068–1072. https://doi.org/10.1126/science.1128845

Pastorello, G., Trotta, C., Canfora, E., Chu, H., Christianson, D., Cheah, Y. W., et al. (2020). The FLUXNET2015 dataset and the ONEFlux processing pipeline for eddy covariance data. *Scientific Data*, *7*(1). https://doi.org/10.1038/s41597-020-0534-3

Penman, H. L. (1948). Natural evaporation from open water, bare soil and grass. *Proceedings of the Royal Society A: Mathematical, Physical & Engineering Sciences*, *193*, 120–145. https://doi.org/10.1098/rspa.1948.0037

Peterson, T., Golubev, V., & Groisman, P. Y. (1995). Evaporation losing its strength. *Nature*, *377*, 687–688. https://doi.org/10.1038/377687b0

Piao, S., Wang, X., Park, T., Chen, C., Lian, X., He, Y., et al. (2019). Characteristics, drivers and feedbacks of global greening. *Nature Reviews Earth & Environment*, *1*(1), 14–27. https://doi.org/10.1038/s43017-019-0001-x

Priestley, C. H. B., & Taylor, R. J. (1972). On the assessment of surface heat flux and evaporation using large-scale parameters. *Monthly Weather Review*, *100*(2), 81–92. https://doi.org/10.1175/1520-0493(1972)100<0081:otaosh>2.3.co;2

Reichstein, M., Falge, E., Baldocchi, D., Papale, D., Aubinet, M., Berbigier, P., et al. (2005). On the separation of net ecosystem exchange into assimilation and ecosystem respiration: Review and improved algorithm. *Global Change Biology*, *11*(9), 1424–1439. https://doi.org/10.1111/j.1365-2486.2005.001002.x

Rodell, M., Beaudoing, H. K., L'Ecuyer, T. S., Olson, W. S., Famiglietti, J. S., Houser, P. R., et al. (2015). The observed state of the water cycle in the early twenty-first century. *Journal of Climate*, *28*(21), 8289–8318. https://doi.org/10.1175/jcli-d-14-00555.1

Rodell, M., Houser, P. R., Jambor, U., Gottschalck, J., Mitchell, K., Meng, C. J., et al. (2004). The global land data assimilation system. *Bulletin of the American Meteorological Society*, *85*(3), 381–394. https://doi.org/10.1175/bams-85-3-381

Roderick, M. L., & Farquhar, G. D. (2004). Changes in Australian pan evaporation from 1970 to 2002. *International Journal of Climatology*, *24*(9), 1077–1090. https://doi.org/10.1002/joc.1061

Sahoo, A. K., Pan, M., Troy, T. J., Vinukollu, R. K., Sheffield, J., & Wood, E. (2011). Reconciling the global terrestrial water budget using satellite remote sensing. *Remote Sensing of Environment*, *115*, 1850–1865. https://doi.org/10.1016/j.rse.2011.03.009
Samaniego, L., Kumar, R., Thober, S., Rakovec, O., Zink, M., Wanders, N., et al. (2017). Toward seamless hydrologic predictions across spatial scales. *Hydrology and Earth System Sciences*, *21*(9), 4323–4346. https://doi.org/10.5194/hess-21-4323-2017
Schlosser, C. A., & Gao, X. (2010). Assessing evapotranspiration estimates from the second global soil wetness project (GSWP-2) simulations. *Journal of Hydrometeorology*, *11*(4), 880–897. https://doi.org/10.1175/2010jhm1203.1
Schneider, T., O'Gorman, P. A., & Levine, X. J. (2010). Water vapor and the dynamics of climate changes. *Reviews of Geophysics*, *48*(3). https://doi.org/10.1029/2009rg000302
Schneider, U., Becker, A., Finger, P., Meyer-Christoffer, A., & Ziese, M. (2018). *GPCC Full data monthly product version 2018 at 0.25°: Monthly land-surface precipitation from rain-gauges built on GTS-based and historical data*. https://doi.org/10.5676/DWD_GPCC/FD_M_V2018_025
Schneider, U., Finger, P., Meyer-Christoffer, A., Rustemeier, E., Ziese, M., & Becker, A. (2017). Evaluating the hydrological cycle over land using the newly-corrected precipitation climatology from the Global Precipitation Climatology Centre (GPCC). *Atmosphere*, *8*(12), 52. https://doi.org/10.3390/atmos8030052
Sheffield, J., Ferguson, C. R., Troy, T. J., Wood, E. F., & McCabe, M. F. (2009). Closing the terrestrial water dget from satellite remote sensing. *Geophysical Research Letters*, *36*(7), L07403. https://doi.org/10.1029/2009GL037338
Sulla-Menashe, D., Gray, J. M., Abercrombie, S. P., & Friedl, M. A. (2019). Hierarchical mapping of annual global land cover 2001 to present: The MODIS Collection 6 Land Cover product. *Remote Sensing of Environment*, *222*, 183–194. https://doi.org/10.1016/j.rse.2018.12.013
Sun, Q., Miao, C., Duan, Q., Ashouri, H., Sorooshian, S., & Hsu, K.-L. (2018). A review of global precipitation datasets: Data sources, estimation, and intercomparisons. *Reviews of Geophysics*, *56*(1), 79–107. https://doi.org/10.1002/2017rg000574
Szilagyi, J. (2014). Temperature corrections in the Priestley–Taylor equation of evaporation. *Journal of Hydrology*, *519*, 455–464. https://doi.org/10.1016/j.jhydrol.2014.07.040
Szilagyi, J. (2018). A calibration-free, robust estimation of monthly land surface evapotranspiration rates for continental-scale hydrology. *Hydrology Research*, *49*(3), 648–657. https://doi.org/10.2166/nh.2017.078
Szilagyi, J. (2021). On the thermodynamic foundations of the complementary relationship of evaporation. *Journal of Hydrology*, *593*, 125916. https://doi.org/10.1016/j.jhydrol.2020.125916
Szilagyi, J., Crago, R., & Ma, N. (2020). Dynamic scaling of the generalized complementary relationship improves long-term tendency estimates in land evaporation. *Advances in Atmospheric Sciences*, *37*(9), 975–986. https://doi.org/10.1007/s00376-020-0079-6
Szilagyi, J., Crago, R., & Qualls, R. (2017). A calibration-free formulation of the complementary relationship of evaporation for continental-scale hydrology. *Journal of Geophysical Research: Atmospheres*, *122*(1), 264–278. https://doi.org/10.1002/2016jd025611
Szilagyi, J., & Jozsa, J. (2008). New findings about the complementary relationship-based evaporation estimation methods. *Journal of Hydrology*, *354*(1–4), 171–186. https://doi.org/10.1016/j.jhydrol.2008.03.008
Szilagyi, J., & Jozsa, J. (2018). Evapotranspiration trends (1979-2015) in the Central Valley of California, USA: Contrasting tendencies during 1981-2007. *Water Resources Research*, *54*(8), 5620–5635. https://doi.org/10.1029/2018WR022704
Szilagyi, J., & Schepers, A. (2014). Coupled heat and vapor transport: The thermostat effect of a freely evaporating land surface. *Geophysical Research Letters*, *41*(2), 435–441. https://doi.org/10.1002/2013gl058979
Tarek, M., Brissette, F. P., & Arsenault, R. (2020). Evaluation of the ERA5 reanalysis as a potential reference dataset for hydrological modelling over North America. *Hydrology and Earth System Sciences*, *24*(5), 2527–2544. https://doi.org/10.5194/hess-24-2527-2020
Trenberth, K. E., Fasullo, J. T., & Kiehl, J. (2009). Earth's global energy budget. *Bulletin of the American Meteorological Society*, *90*(3), 311–324. https://doi.org/10.1175/2008bams2634.1
Trenberth, K. E., Smith, L., Qian, T., Dai, A., & Fasullo, J. (2007). Estimates of the global water budget and its annual cycle using observational and model data. *Journal of Hydrometeorology*, *8*(4), 758–769. https://doi.org/10.1175/jhm600.1
Twine, T. E., Kustas, W. P., Norman, J. M., Cook, D. R., Houser, P. R., Meyers, T. P., et al. (2000). Correcting eddy-covariance flux underestimates over a grassland. *Agricultural and Forest Meteorology*, *103*, 279–300. https://doi.org/10.1016/s0168-1923(00)00123-4
Van Looy, K., Bouma, J., Herbst, M., Koestel, J., Minasny, B., Mishra, U., et al. (2017). Pedotransfer functions in Earth system science: Challenges and perspectives. *Reviews of Geophysics*, *55*(4), 1199–1256. https://doi.org/10.1002/2017rg000581
Vinukollu, R. K., Meynadier, R., Sheffield, J., & Wood, E. F. (2011). Multi-model, multi-sensor estimates of global evapotranspiration: Climatology, uncertainties and trends. *Hydrological Processes*, *25*, 3993–4010. https://doi.org/10.1002/hyp.8393
Wang-Erlandsson, L., van der Ent, R. J., Gordon, L. J., & Savenije, H. H. G. (2014). Contrasting roles of interception and transpiration in the hydrological cycle – Part 1: Temporal characteristics over land. *Earth System Dynamics*, *5*(2), 441–469. https://doi.org/10.5194/esd-5-441-2014
Wang, K., & Dickinson, R. E. (2012). A review of global terrestrial evapotranspiration: Observation, modeling, climatology, and climatic variability. *Reviews of Geophysics*, *50*(2). https://doi.org/10.1029/2011rg000373
Watkins, M. M., Wiese, D. N., Yuan, D., Boening, C., & Landerer, F. W. (2015). Improved methods for observing Earth's time variable mass distribution with GRACE using spherical cap mascons. *Journal of Geophysical Research: Solid Earth*, *120*(4), 2648–2671. https://doi.org/10.1002/2014JB011547
Weedon, G. P., Balsamo, G., Bellouin, N., Gomes, S., Best, M. J., & Viterbo, P. (2015). The WFDEI meteorological forcing data set: WATCH Forcing Data methodology applied to ERA-Interim reanalysis data. *Water Resources Research*, *50*(9), 7505–7514. https://doi.org/10.1002/2014WR015638
Wei, Y., Liu, S., Huntzinger, D. N., Michalak, A. M., Viovy, N., Post, W. M., et al. (2014). The North American carbon program multi-scale synthesis and terrestrial model intercomparison project-part 2: Environmental driver data. *Geoscientific Model Development*, *7*(6), 2875–2893. https://doi.org/10.5194/gmd-7-2875-2014
Wild, M., Folini, D., Hakuba, M. Z., Schär, C., Seneviratne, S. I., Kato, S., et al. (2015). The energy balance over land and oceans: An assessment based on direct observations and CMIP5 climate models. *Climate Dynamics*, *44*(11–12), 3393–3429. https://doi.org/10.1007/s00382-014-2430-z
Wilkinson, K., Zabern, M. v., & Scherzer, J. (2014). *Global freshwater fluxes into the world oceans* (p. 9). Neustadt/Weinstraße.
Willett, K. M., Gillett, N. P., Jones, P. D., & Thorne, P. W. (2007). Attribution of observed surface humidity changes to human influence. *Nature*, *449*(7163), 710–712. https://doi.org/10.1038/nature06207
Xu, C., & Singh, V. P. (2005). Evaluation of three complementary relationship evapotranspiration models by water balance approach to estimate actual regional evapotranspiration in different climatic regions. *Journal of Hydrology*, *308*, 105–121. https://doi.org/10.1016/j.jhydrol.2004.10.024
Xu, Z., Jiang, Y., Jia, B., & Zhou, G. (2016). Elevated-CO_2 response of stomata and its dependence on environmental factors. *Frontiers in Plant Science*, *7*, 657. https://doi.org/10.3389/fpls.2016.00657
Zektser, I. S., Everett, L. G., & Dzhamalov, R. G. (2006). *Submarine groundwater*. CRC Press.

Zeng, Z., Peng, L., & Piao, S. (2018). Response of terrestrial evapotranspiration to Earth's greening. *Current Opinion in Environmental Sustainability*, *33*, 9–25. https://doi.org/10.1016/j.cosust.2018.03.001

Zeng, Z., Piao, S., Li, L. Z. X., Wang, T., Ciais, P., Lian, X., et al. (2018). Impact of Earth greening on the terrestrial water cycle. *Journal of Climate*, *31*(7), 2633–2650. https://doi.org/10.1175/jcli-d-17-0236.1

Zeng, Z., Wang, T., Zhou, F., Ciais, P., Mao, J., Shi, X., & Piao, S. (2014). A worldwide analysis of spatiotemporal changes in water balance-based evapotranspiration from 1982 to 2009. *Journal of Geophysical Research: Atmospheres*, *119*, 1186–1202. https://doi.org/10.1002/2013jd020941

Zhang, K., Kimball, J. S., Nemani, R. R., Running, S. W., Hong, Y., Gourley, J. J., & Yu, Z. (2015). Vegetation greening and climate change promote multidecadal rises of global land evapotranspiration. *Scientific Reports*, *5*, 15956. https://doi.org/10.1038/srep15956

Zhang, K., Zhu, G., Ma, J., Yang, Y., Shang, S., & Gu, C. (2019). Parameter analysis and estimates for the MODIS evapotranspiration algorithm and multiscale verification. *Water Resources Research*, *55*(3), 2211–2231. https://doi.org/10.1029/2018wr023485

Zhang, Y., Kong, D., Gan, R., Chiew, F. H. S., McVicar, T. R., Zhang, Q., & Yang, Y. (2019). Coupled estimation of 500 m and 8-day resolution global evapotranspiration and gross primary production in 2002–2017. *Remote Sensing of Environment*, *222*, 165–182. https://doi.org/10.1016/j.rse.2018.12.031

Zhang, Y., Liu, C., Tang, Y., & Yang, Y. (2007). Trends in pan evaporation and reference and actual evapotranspiration across the Tibetan Plateau. *Journal of Geophysical Research*, *112*(D12110). https://doi.org/10.1029/2006JD008161

Zhang, Y., Pena-Arancibia, J. L., McVicar, T. R., Chiew, F. H., Vaze, J., Liu, C., et al. (2016). Multi-decadal trends in global terrestrial evapotranspiration and its components. *Scientific Reports*, *6*, 19124. https://doi.org/10.1038/srep19124

Zheng, H., Yang, Z.-L., Lin, P., Wei, J., Wu, W.-Y., Li, L., et al. (2019). On the sensitivity of the precipitation partitioning into evapotranspiration and runoff in land surface parameterizations. *Water Resouces Research*, *55*, 95–111. https://doi.org/10.1029/2017WR022236

Zhu, Z., Piao, S., Myneni, R. B., Huang, M., Zeng, Z., Canadell, J. G., et al. (2016). Greening of the Earth and its drivers. *Nature Climate Change*, *6*(8), 791–795. https://doi.org/10.1038/nclimate3004

Erratum

In the originally published version of this article, in Figure 12, the black line of the CR data was shifted backward by one year. The figure has been updated and this version may be considered the authoritative version of record.